# Petrological Evolution of the Magmatic Suite Associated with the Coroccohuayco Cu(–Au–Fe) Porphyry–Skarn Deposit, Peru

Cyril Chelle-Michou[1],*, Massimo Chiaradia[1], Paul Béguelin[1] and Alexey Ulianov[2]

[1]Department of Earth Sciences, University of Geneva, Rue des Maraîchers 13, 1205 Geneva, Switzerland and [2]Institute of Earth Sciences, University of Lausanne, Geopolis, 1015 Lausanne, Switzerland

*Corresponding author. E-mail: cyril.chelle-michou@unige.ch

## ABSTRACT

The petrological evolution of magmatic rocks associated with porphyry-related Cu deposits is thought to exert a first-order control on ore genesis. It is therefore critical to understand and recognize petrological processes favourable to the genesis of porphyry systems. In this study we present new petrographic, geochemical (whole-rock and mineral), and isotopic (Pb, Sr, Nd) data for rocks from the magmatic suite associated with the Eocene Coroccohuayco porphyry–skarn deposit, southern Peru. Previously determined radiometric ages on these rocks provide the temporal framework for interpretation of the data. Arc-style magmatic activity started at Coroccohuayco with the emplacement of a composite precursor gabbrodiorite complex at *c.* 40·4 Ma. After a nearly 5 Myr lull, magmatic activity resumed at *c.* 35·6 Ma with the rapid emplacement of three dacitic porphyries associated with mineralization. However, zircon antecrysts in the porphyries show that intra-crustal magmatic activity started *c.* 2 Myr before porphyry emplacement and probably built a large intra-crustal magmatic body with an associated large thermal anomaly. Our data suggest that all magmas underwent a period of evolution in the deep crust before transfer and further evolution in the upper crust. The gabbrodiorite complex was sourced from a heterogeneous deep crustal reservoir and was emplaced at a pressure of 100–250 MPa where it underwent a limited amount of fractionation and formed a chemically zoned pluton. Its initial water content and oxygen fugacity were estimated to be around 3 wt % $H_2O$ and NNO $\pm$ 1 (where NNO is the nickel–nickel oxide buffer), respectively. The deep crustal source of the porphyries appears to have been more homogeneous. The porphyries are interpreted to be the product of advanced differentiation of a parental magma similar to the gabbrodiorite. Most of this evolution occurred at deep crustal levels (around 800 MPa) through fractionation of amphibole + pyroxene + plagioclase $\pm$ garnet, leading to the development of a high Sr/Y signature characteristic of porphyry-related magmatism worldwide. Subsequent upper crustal evolution (100–250 MPa) was dominated by crustal assimilation, cannibalism of previously emplaced magma batches (proto-plutons) and magma recharge. Water content and oxygen fugacity were estimated to be around 5 wt % $H_2O$ and NNO + 1 to NNO + 2, respectively, at the end of the period of upper crustal evolution. This high oxygen fugacity is inferred to have favoured sulphur and metal enrichment in the melt. The high thermal regime generated through 2 Myr of sustained magmatism in the upper crust favoured crustal assimilation, proto-pluton cannibalism, and efficient metal extraction upon fluid exsolution. The Coroccohuayco magmatic suite appears to have acquired its metallogenic potential (high $fO_2$, high Sr/Y) through several million years of deep crustal evolution.

Key words: deep crustal evolution; high Sr/Y magma; magma fertility; porphyry Cu deposit; proto-pluton cannibalism

## INTRODUCTION

Porphyry systems (porphyry Cu–Mo–Au, Cu–Zn–Pb–Au skarn, Cu–Zn–Pb–Au–Ag epithermal) result from the focused release of saline metal- and sulphur-bearing hydrothermal fluids from a cooling upper crustal magma chamber (e.g. Sillitoe, 2010). These systems are regarded as the result of the positive interplay between tectonic, magmatic and hydrothermal processes (Tosdal & Richards, 2001; Richards, 2013). They commonly occur in Cenozoic to Mesozoic fossil magmatic arcs, although some older examples are also found. Because magmas are recognized as the source of most of the metals and fluids (Hedenquist & Lowenstern, 1994; Dreher *et al.*, 2005; Pettke *et al.*, 2010; Simon & Ripley, 2011; Stern *et al.*, 2011) it is critical to understand how a magmatic system will become productive and ultimately favour the genesis of economic mineralization. The common association of high Sr/Y magma with porphyry systems (Sr/Y > 20–40; Thiéblemont *et al.*, 1997; Sajona & Maury, 1998; Oyarzun *et al.*, 2001; Rohrlach & Loucks, 2005; Richards & Kerrich, 2007; Shafiei *et al.*, 2008; Chiaradia *et al.*, 2009*a*; Hou *et al.*, 2009; Shen *et al.*, 2009; Schütte *et al.*, 2010; Richards *et al.*, 2012; Loucks, 2014) suggests that specific petrological processes play a key role in the genesis of economic mineralization.

Many studies have highlighted the importance of deep crustal petrological processes in producing hydrous, oxidized, S-rich, metal-rich and high Sr/Y magmas associated with porphyry systems (e.g. Richards, 2011*a*, 2011*b*, and references therein). However, others have proposed that petrological processes happening in an upper to mid-crustal magma chamber may be of primary importance. Such processes may involve the following: (1) mafic magma underplating and degassing significant amounts of sulphur- and metal-rich magmatic fluids into an overlying felsic magma (Keith *et al.*, 1997; Hattori & Keith, 2001; de Hoog *et al.*, 2004; Blundy *et al.*, 2015); (2) saturation of magmatic sulphides followed by remobilization through their destabilization by magmatic–hydrothermal fluids (Keith *et al.*, 1997; Halter *et al.*, 2002, 2005; Nadeau *et al.*, 2010; Wilkinson, 2013).

Here we present a detailed petrological study of the Eocene magmatic suite associated with the Coroccohuayco porphyry–skarn Cu(–Au–Fe) deposit, southern Peru. Studies of magmatic systems associated with porphyry ore deposits aim at reconstructing the depth- and time-integrated evolutionary path (in terms of pressure, temperature and chemical composition) of magma from genesis to emplacement. However, at most fossil porphyry systems (such as Coroccohuayco) the available part of the magmatic system (porphyry stocks and dykes) represents only a very small window to study petrological processes through the entire continental crust. Indeed, porphyritic rocks at ore depth typically represent small apophyses episodically extruded from a much larger pluton lying at greater depth.

At Coroccohuayco magmatism spans nearly 5 Myr and temporally evolves from basic to silicic, although only the late silicic stages are directly linked to ore genesis (Chelle-Michou *et al.*, 2014, 2015). Such a long-lived system offers the opportunity to provide a time-constrained perspective on the petrological evolution of a porphyry system. We use petrographic observations, major and trace element geochemistry of minerals and whole-rocks, radiogenic isotopes of whole-rocks (Pb, Sr, Nd), trace element modelling, and previously published ages (Chelle-Michou *et al.*, 2014, 2015) to provide a time-resolved reconstruction of the evolution of intensive parameters ($P$–$T$–$H_2O$–$fO_2$) and the geochemistry of the magmatic system. Ultimately, we aim to constrain the locus and processes of magma generation and evolution and to understand their impact on the genesis of the Cu(–Au–Fe) porphyry–skarn mineralization.

## EOCENE GEODYNAMIC SETTING, ARC MAGMATISM AND PORPHYRY SYSTEMS IN SOUTHERN PERU

The Coroccohuayco porphyry–skarn deposit is part of the Tintaya mining district (which also includes the deposits of Tintaya and Antapaccay) located at the southern edge of the Eocene Andahuaylas–Yauri batholith in southern Peru (inset Fig. 1; Perelló *et al.*, 2003; Maher, 2010). This batholith has recently emerged as an important metallogenic belt, owing to major discoveries of world-class porphyry copper systems (e.g. Antapaccay, Las Bambas).

During the Eocene period flattening of the subducting Nazca slab in the Central Andean Zone resulted in a northeastward inland migration (up to 200 km) of the magmatic arc compared with its previous positions (inset Fig. 1; Mamani *et al.*, 2010). This timing also corresponds to the Incaic compressional event that initiated crustal-scale thickening and shortening in the central Andes (Sandeman *et al.*, 1995; Carlotto, 1998; Mamani *et al.*, 2010), oroclinal bending (Roperch *et al.*, 2006, 2011; Arriagada *et al.*, 2008) and the initial phase of building of the Altiplano (McQuarrie *et al.*, 2005). As crustal thickening, shortening, bending and uplift continued in the central Andes, the Nazca plate motion vector changed at *c.* 28–25 Ma to become normal and the convergence rate increased (Somoza & Ghidella, 2012). The angle of subduction has steepened and the magmatic arc has slowly migrated trenchward from then on (inset Fig. 1; Mamani *et al.*, 2010).

The Andahuaylas–Yauri batholith is the plutonic remnant of this Eocene calc-alkaline magmatic arc (Mamani *et al.*, 2010), and is continuous to the south with the Chilean Eocene magmatic arc along the Cordillera de Domeyco that hosts some of the largest porphyry systems in the world (Perelló *et al.*, 2003). It now forms a 300 km long and up to 130 km wide batholith emplaced into Mesozoic to early Cenozoic marine sedimentary
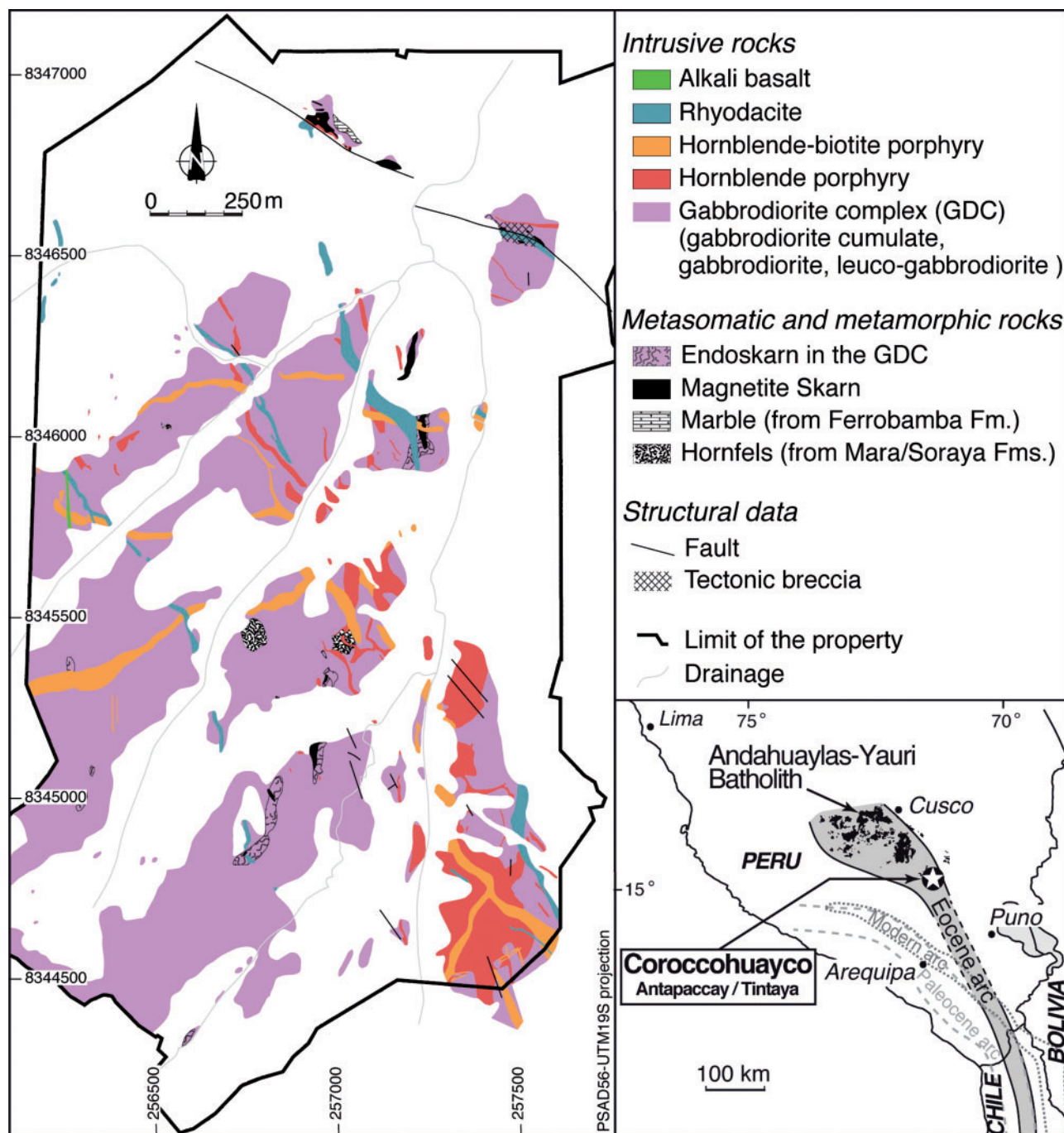
**Fig. 1.** Geological map of the Coroccohuayco prospect. Inset shows the location of the Andahuaylas–Yauri Batholith and the southward extension of the Eocene arc in Chile.

sequences. In a regional study, Perelló *et al.* (2003) identified an early dominantly mafic phase of magmatism followed by a dominantly felsic one, the latest being locally associated with porphyry systems.

The Tintaya district represents a tectonically uplifted window of Mesozoic basement surrounded by Cenozoic volcano-sedimentary basins. It was affected by two phases of Eocene magmatic activity that intruded Cretaceous sandstones and limestones. Cu–Fe-rich skarn-type mineralization is commonly found at

the contact between the felsic porphyritic rocks and the Cretaceous limestone (Ferrobamba formation) throughout the district.

## GEOLOGY OF COROCCOHUAYCO AND ITS MAGMATIC SUITE

Like porphyry-related magmatism elsewhere (Sillitoe, 2010), Coroccohuayco records poly-phasic magmatic activity (Fig. 1 and Fig. 2). From ~40·4 Ma to 40·2 Ma a

heterogeneous, dominantly mafic complex termed the gabbrodiorite complex (GDC) was emplaced (Chelle-Michou *et al.*, 2014). It is mainly composed of hornblende gabbro and diorite with subordinate amounts of their leucocratic equivalents and very minor anorthosite. The GDC crops out continuously over an area of $\sim$10 km$^2$. Drill-hole intersections show that, at least just above the Coroccohuayco skarn ore body, it is emplaced as an $\sim$250 m thick sill-like intrusion capping Cretaceous limestones, with local deeper roots (Chelle-Michou *et al.*, 2015). The total preserved volume of this complex is estimated to be in the range of 3–10 km$^3$.

After a nearly 5 Myr lull, magmatism resumed with the sequential intrusion of three porphyries of dacitic to rhyodacitic composition at around 35·6 Ma (Chelle-Michou *et al.*, 2014). This started with the emplacement of stocks and NW–SE- and ENE–WSW-trending dykes of hornblende-bearing porphyry, closely followed by a hornblende- and biotite-bearing porphyry. On the basis of high-precision U–Pb geochronology, Chelle-Michou *et al.* (2014) estimated that the porphyries were emplaced in less than 86 kyr. They are temporally and genetically related to the ore-forming hydrothermal event (Chelle-Michou *et al.*, 2015). These first two porphyries were subsequently crosscut by subvolcanic NW–SE-trending rhyodacite porphyry dykes marking the end of the Eocene magmatism at Coroccohuayco. Although the rhyodacite commonly displays pervasive hydrothermal alteration, it postdates the main ore stage. Its emplacement age could not be resolved precisely, but it is believed to have intruded in the 35·6–35·0 Ma time interval (Chelle-Michou *et al.*, 2014). Zircon antecrysts in the three porphyries indicate that deep-seated magmatism had actually resumed by $\sim$37·5 Ma, and continued until the emplacement of the rhyodacite at upper crustal levels (Chelle-Michou *et al.*, 2014). This sustained 2 Myr period of intra-crustal magmatic activity led to the building of a stable thermal anomaly that may have favoured cannibalization of previously emplaced magma batches (proto-plutons) and crustal assimilation (Chelle-Michou *et al.*, 2014). Using the zircon Ce/Nd ratio as a proxy for magma oxidation state (similar to the zircon Ce anomaly or zircon Ce$^{4+}$/Ce$^{3+}$ ratio), Chelle-Michou *et al.* (2014) showed that the porphyries (Ce/Nd of 9–46) are significantly more oxidized than the GDC (Ce/Nd of 2–12). For Eocene zircons from the porphyries (autocrysts and antecrysts spanning the *c.* 37·5–35·6 Ma age interval), they also noted an absence of correlation between zircon Ce/Nd and age, suggesting that the oxidized character of the magma was already established at 37·5 Ma and persisted until the emplacement of the porphyries at 35·6 Ma.

Magmatism at Coroccohuayco finally terminated at $\sim$26·6 Ma with the intrusion of north–south-trending dykes of clinopyroxene-bearing alkali basalt (Chelle-Michou *et al.*, 2015). Because of its temporal relationship with the other magmatic rock, the alkali basalt is not considered to be part of the Coroccohuayco

magmatic suite. Instead, it is temporally related to the Tacaza arc that marked the beginning of the trenchward migration of arc magmatism in southern Peru (see Mamani *et al.*, 2010).

## SAMPLES AND ANALYTICAL METHODS

Rock samples were collected from both outcrops and drillcore. Only the least hydrothermally altered samples of each rock type were selected for geochemical and isotopic analysis on the basis of hand lens and thin section observations. However, all samples of the rhyodacite display extensive alteration of mafic minerals and moderate to pervasive sericitization of plagioclase and groundmass. To constrain crustal assimilation, we also included three Triassic red-bed samples of the Mitu group from the Mamuera section (60 km NE of Coroccohuayco; Reitsma, 2012). On the basis of xenocrystic zircon age distribution and Hf isotopes, such sediments have been proposed as assimilants for the porphyries (Chelle-Michou *et al.*, 2014).

Approximate modal mineral abundances were obtained from image analysis of scanned thin sections with an estimated uncertainty of <1% (>1000 points).

Microprobe analysis of amphibole, pyroxene, plagioclase and K-feldspar [Supplementary Data (SD) Tables 1–4; supplementary data are available for downloading at http://www.petrology.oxfordjournals.org] were carried out at the University of Lausanne on a JEOL 8200 electron microprobe equipped with five wavelength-dispersive spectrometers. We employed an accelerating voltage of 15 kV, a beam current of 15 nA, a spot size of 3 $\mu$m and measuring time of 10–30 s on peak and half this time on the respective backgrounds before and after the peak depending on the element and the mineral analysed. Both natural and synthetic silicates, oxides and sulphate standards were used for external calibration.

*In situ* trace element abundances in amphibole, plagioclase and pyroxenes (SD Tables 1–4) were determined on polished thin sections by laser ablation inductively coupled plasma mass spectrometry (LA-ICP-MS) using a Thermo ELEMENT XR sector-field ICP-MS system interfaced to a UP-193FX ArF excimer laser ablation system at the Institute of Earth Sciences of the University of Lausanne. The mass spectrometer optimization was similar to that described by Ulianov *et al.* (2012). Operating conditions of the ablation system included a repetition rate of 12 Hz, a pit size of 35–50 $\mu$m and an on-sample energy density of 5·0 J cm$^{-2}$. The NIST standard glass SRM 612 was employed for external standardization. SiO$_2$ and CaO determined by electron microprobe analysis on the same spot as subsequent ablation served as an internal standard for feldspars (plagioclase, K-feldspar) + orthopyroxene and amphibole + clinopyroxene, respectively. Raw data were reduced off-line using the LAMTRACE software (Jackson, 2008). The reproducibility (1$\sigma$) of the measured trace element abundances in the SRM 612 glass

standard generally range from <1 relative % (rel. %) to <10 rel. %, depending on the element and the analytical list (feldspar or amphibole).

Whole-rock samples were crushed using a steel jaw crusher and powdered with an agate mill (<70 μm). Fused glass beads (fluxed with $Li_2B_4O_7$) and pressed powder pellets from whole-rock powders were analysed for major, minor and some trace elements by X-ray fluorescence (XRF) at the University of Lausanne (Table 2, SD Table 5). Data quality was controlled with the BHVO, NIM-N, NIM-G, SY-2, SDC-1 and QLO standards. Average reproducibility (1σ) of major and trace elements on these standards is <1 rel. % for all major elements (except for MgO and $K_2O$, <3 rel. %) and <10 rel. % for trace elements (<0·3 rel. % for Sr). Rare earth elements (REE) and additional trace elements were analysed by LA-ICP-MS on fused glass bead (Table 2, SD Table 5) fragments previously used for XRF analysis. Analysis were carried out at the University of Lausanne either on a Thermo ELEMENT XR sector-field ICP-MS system interfaced to an UP-193FX ArF excimer laser ablation system or a Perkin–Elmer ELAN 6100 DRC quadrupole ICP-MS system interfaced to a GeoLas 200M 193 nm Lambda Physik excimer laser ablation system. Operating conditions of the ablation systems included a repetition rate of 15 or 10 Hz, a pit size of 100 or 120 μm and an on-sample energy density of 5·0 or 16·8 J cm$^{-2}$ depending on the equipment used. The NIST standard glass SRM 612 was employed for external standardization and the Sr content determined by XRF for each sample served as an internal standard. Raw data were reduced off-line using the LAMTRACE software (Jackson, 2008). For each sample three points were measured and results were averaged. The reproducibility (1σ) of the measured trace element abundances in the SRM 612 glass standard was <3 rel. % for all elements whereas reproducibilities of repeated analysis on the same sample are <10% for all elements (decreasing uncertainty with increasing element content).

Selected whole-rock samples were analysed for their Sr, Nd and Pb isotopic composition (Table 2; SD Table 5) at the University of Geneva. About 120 mg of powdered rock was dissolved over 7 days using a mixture of 4 ml conc. HF and 1 ml 15M $HNO_3$ in Teflon vials on a hot plate (140°C). The sample was then dried on a hot plate, dissolved again in 3 ml of 15M $HNO_3$ in closed Teflon vials at 140°C and dried down again. Sr, Nd and Pb separation was carried out using cascade columns with Sr-spec, TRU-spec and Ln-spec resins following a modified method after Pin *et al.* (1994). Pb was further purified with an AG-MP1-M anion exchange resin in a hydrobromic medium. Pb, Sr and Nd isotope ratios were measured either on a Thermo TRITON mass spectrometer or on a Thermo NEPTUNE Plus mass spectrometer at the University of Geneva, following methods described by Chiaradia *et al.* (2014) and Béguelin *et al.* (2015), respectively.

# PETROGRAPHY AND MINERAL CHEMISTRY

## Gabbrodiorite complex (GDC)

Rocks from the GDC are mainly composed of plagioclase, calcic amphibole, Fe–Ti oxides and minor amounts of clinopyroxene and/or orthopyroxene with variable mineral proportions and grain sizes (Fig. 2). Accessory phases include quartz, K-feldspar, zircon, apatite, and minor titanite and biotite. Plagioclase is euhedral to subhedral and normally zoned, with Ca-richer cores and Ca-poorer rims (Fig. 3a and b). Amphibole crystals are commonly overgrown on a resorbed core of either clinopyroxene or orthopyroxene (Fig. 3c and d). Clinopyroxene cores tend to be more resorbed and skeletal than orthopyroxene cores and are sometimes hydrated and replaced by tremolite–actinolite. Amphibole is always poikilitic and encloses plagioclase and Fe–Ti oxides (Fig. 3b–e). Quartz, sodic plagioclase, Fe–Ti oxides (magnetite and ilmenite), K-feldspar, apatite, zircon and sparse interstitial titanite and biotite fill the inter-mineral spaces (Fig. 3a and b).

The modal mineralogy of each sample (SD Table 5) highlights the diversity of the GDC. Modal amphibole and plagioclase contents are inversely correlated and vary from 58·1 to 13·7 vol. % and from 78·0 to 37·2 vol. %, respectively. The textural and mineralogical heterogeneity of the gabbrodiorite complex is also observed at the hand sample scale. For example, clinopyroxene- and orthopyroxene-bearing (in the core of amphiboles) zones locally form banded textures (Fig. 3e). Similarly, coarser grained zones and finer grained zones or zones richer or poorer in mafic minerals are locally observed next to each other, with sharp and sinuous contacts (Fig. 3f).

On the basis of modal abundances of plagioclase and amphibole (Table 1) as well as whole-rock Eu anomalies (see below), we have subdivided the GDC into three units: (1) 'gabbrodiorite cumulate' (the cumulate nature of this unit is discussed below) characterized by positive Eu anomalies and an amphibole-rich mineralogy (>31 vol. %); (2) 'gabbrodiorite' *sensu stricto*, defined by the absence of Eu anomalies and a modal amphibole content of 28–33 vol. %; (3) 'leuco-gabbrodiorite', with no Eu anomaly and modal amphibole content of 10–20 vol. %. Contacts between the gabbrodiorite 'cumulate' and the gabbrodiorite were not observed in the field and their respective distribution could not be clearly established. However, the gabbrodiorite 'cumulate' appears to be dominant toward the southern part of Coroccohuayco. The bodies of leuco-gabbrodiorite are typically small (10 m$^2$ in outcrop area) and their 3D geometry is unclear. They intrude the gabbrodiorite and gabbrodiorite 'cumulates' with all of which they display sharp contacts.

## Plagioclase

At the hand sample scale plagioclase displays a wide range of compositions from An90 in some cores to as low as An15 in the inter-mineral space (Fig. 4b–g). Most
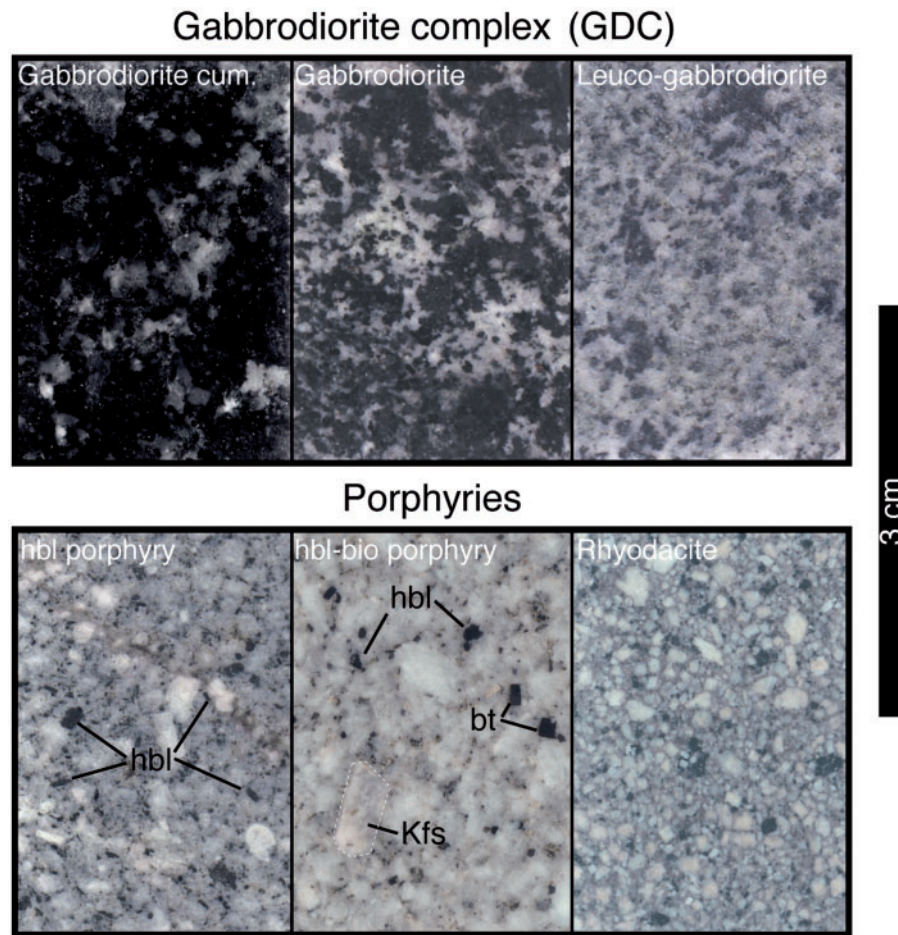
**Fig. 2.** Photographs of the magmatic rock types encountered at Coroccohuayco. bt, biotite; cum, cumulate; hbl, hornblende; Kfs, K-feldspar.

plagioclase crystals are normally zoned with a broad homogeneous core and relatively thin rims of increasingly albitic composition. The few anorthite-rich cores (>An85) are rounded and overgrown with sharp contacts by lower An rims. In each sample, plagioclase displays one or two dominant compositional modes with higher and lower An contents corresponding to the inner core(s) and the rim(s), respectively (Fig. 4b–g). The plagioclase composition in the gabbrodiorite 'cumulates' is mostly An75–70 and An60–55, whereas plagioclase in the gabbrodiorite is mostly An60–55 (with some deviation towards higher and lower values). Plagioclases in the leuco-gabbrodiorite are the most evolved with a compositional mode at An35–30.

On trace element profiles, the REE (in particular La) are inversely correlated with An content (Fig. 4b–g).

### Hornblende
Amphiboles of the GDC are Mg-rich [Mg# > 0·5, where Mg# = Mg/(Mg + Fe$^{2+}$)] and calcic (Ca$_B$ ≥ 1·5). In the classification scheme of Leake *et al.* (1997), most amphiboles are magnesio-hornblendes [6·5 < Si < 7·5; (Na + K)$_A$ < 0·5], with a few outliers lying in the fields of tschermakite [5·5 < Si < 6·5; (Na + K)$_A$ < 0·5] and less commonly magnesio-hastingsite [6·5 < Si < 7·5;

(Na + K)$_A$ ≥ 0·5; $^{VI}$Al < Fe$^{3+}$; Fig. 5a and b]. Slightly fluid-altered hornblendes have bleached colors and their composition shifts toward the field of actinolite and tremolite (Si > 7·5) as a result of Fe depletion and Ca and Si addition.

For 'fresh' amphiboles, Mg# varies from 0·94 to 0·64; Al$_T$ varies from 0·8 to 2·0 p.f.u. and correlates positively with (Na + K)$_A$ ($r$ = 0·89), Al$_{VI}$ ($r$ = 0·70; Fig. 5a–c) and most compatible and incompatible trace elements including Sr, Ba, Y, Ta and REE (Fig. 6a–e). In detail, some trace elements (e.g. Zr) define at least two groups of amphiboles at the sample (thin section) scale (Fig. 6c). Hornblendes from the gabbrodiorite exhibit slightly lower Sr/Y values (∼0·7) than amphiboles from the gabbrodiorite 'cumulate' (∼1·5), and both have (La/Yb)$_N$ values around unity (Fig. 6d and e).

### Pyroxene
Clinopyroxene hosted in the core of amphibole plots at the diopside–augite boundary and has Mg# [Mg# = Mg/(Mg + Fe$_{tot}$)] of 0·73–0·79; Al$_T$ varies from 0·014 to 0·056 p.f.u. (SD Table 3). Orthopyroxene hosted in the core of amphibole has a composition ranging from En54 to En63, Mg# of 0·57–0·66 and Al$_T$ of
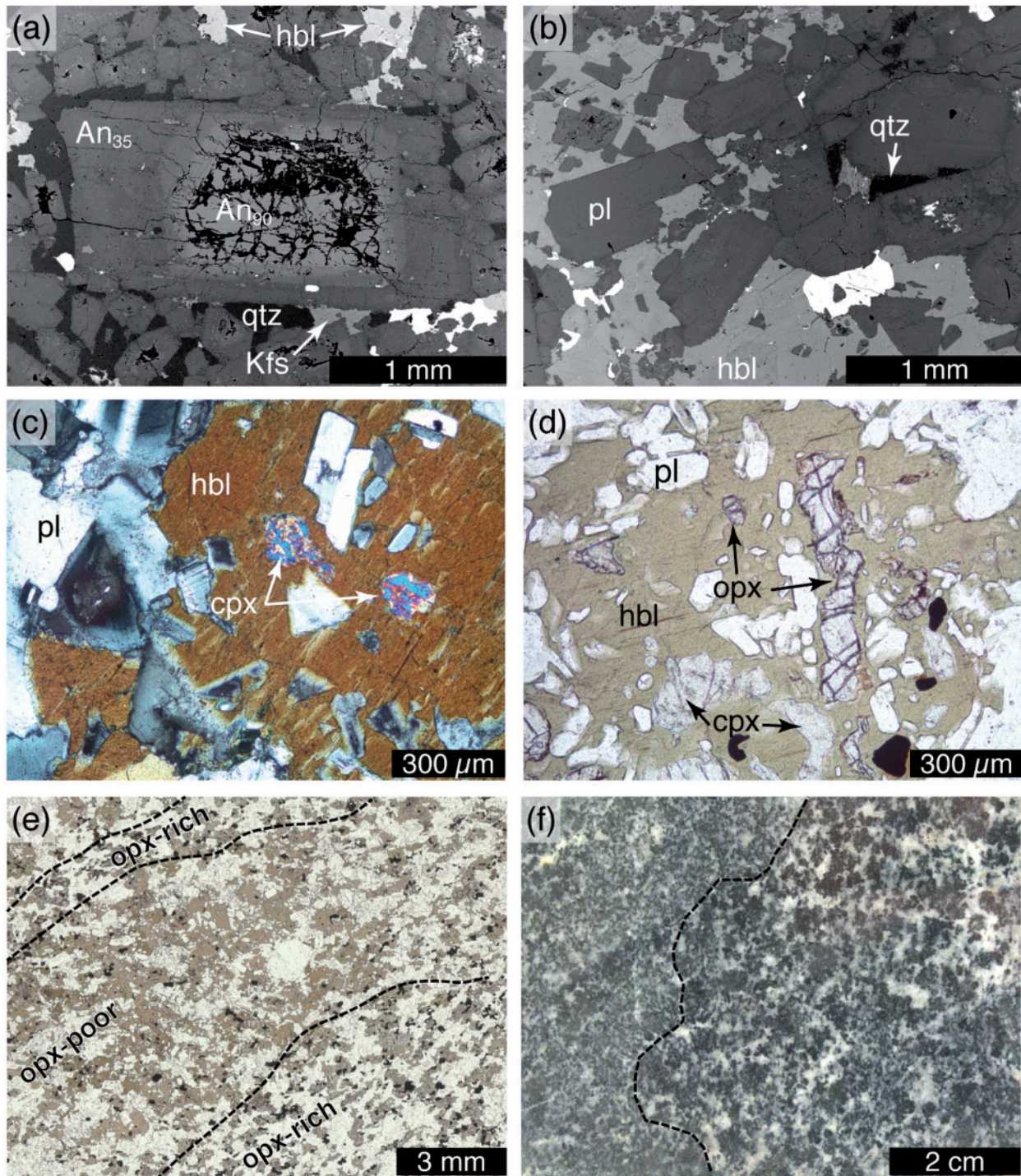
**Fig. 3.** Photomicrographs of samples from the gabbrodiorite complex. (a) Back-scattered electron (BSE) image of zoned plagioclase with an anorthite-rich core overgrown by more sodic plagioclase. Hornblende, K-feldspar, quartz and Fe–Ti oxides are interstitial between the plagioclase crystals. (b) BSE image of plagioclase with slightly more sodic rim compared with the core, enclosed in a hornblende oikocryst. (c) Amphibole oikocryst with resorbed skeletal clinopyroxene in the core (cross-polarized light). (d) Amphibole oikocryst containing resorbed orthopyroxene and clinopyroxene (plane-polarized light). (e) Orthopyroxene-rich and -poor zones displaying banding (thin section scan). (f) Sharp contact between fine- and coarse-grained gabbrodiorite. cpx, clinopyroxene; hbl, hornblende; Kfs, K-feldspar; opx, orthopyroxene; pl, plagioclase; qtz, quartz.

0·027–0·088 p.f.u. (SD Table 4). Both pyroxenes display a negative Eu anomaly in chondrite-normalized REE patterns (Fig. 7). Clinopyroxene is characterized by depletion of light REE (LREE) compared with middle REE (MREE) and heavy REE (HREE).

**Porphyries**

The three types of porphyritic rock are distinguished on the basis of phenocryst content and groundmass–phenocryst proportions (Table 1, Fig. 2). The groundmass consists of a microcrystalline patchwork of quartz,

**Table 1**: Average modal composition (vol. %) of rocks units from the Coroccohuayco magmatic suite

| Rock type: | Gabbrodiorite complex | | | Porphyries | | | |
|---|---|---|---|---|---|---|---|
| | Gabbro-diorite cumulate ($n = 6$) | Gabbro-diorite ($n = 5$) | Leuco-gabbro-diorite ($n = 2$) | hbl porphyry ($n = 7$) | hbl–bio porphyry ($n = 4$) | hbl–bio porphyry chilled margin ($n = 2$) | Rhyodacite ($n = 4$) |
| Groundmass/ interstitial pockets | ~1·0 | ~1·0 | ~1·0 | 49·8 (1·5) | 46·5 (1·5) | 55·8 (0·8) | 56·2 (2·3) |
| Hornblende | 38·1 (9·9) | 30·4 (1·8) | 15·9 (2·1) | 9·9 (2·9) | 6·1 (2·1) | 4·6 (0·9) | 2·8 (0·8) |
| Biotite | | 0·6 (0·8) | | 0·4 (0·4) | 1·2 (0·4) | 1·0 (0·2) | 1·7 (0·5) |
| Clinopyroxene/ actinolite | 0·7 (0·0) | 0·5 (0·0) | | | | | |
| Orthopyroxene | 2·2 (2·9) | | 2·8 (2·9) | | | | |
| Plagioclase | 53·7 (9·1) | 62·7 (1·6) | 77·8 (0·3) | 37·5 (3·6) | 43·6 (1·3) | 36·3 (1·8) | 37·4 (1·9) |
| K-feldspar | | | | 0·2 (0·1) | 1·4 (0·8) | 0·9 (0·1) | 0·9 (0·9) |
| Fe–Ti oxides | 4·3 (0·5) | 4·7 (1·3) | 2·6 (0·5) | 1·4 (0·2) | 0·8 (0·2) | 0·9 (0·1) | 0·7 (0·2) |
| Titanite | | 0·1 (0·2) | | 0·6 (0·2) | 0·3 (0·0) | 0·3 (0·0) | |
| Apatite | | | | 0·2 (0·1) | 0·1 (0·0) | 0·2 (0·1) | 0·3 (0·1) |

Values in parentheses are 1SD.

albitic plagioclase and K-feldspar. The main mineral phases are hornblende, plagioclase, magnetite, biotite and K-feldspar. Zircon and apatite are common accessory minerals in all three porphyries, whereas titanite is observed only in the hornblende and hornblende–biotite porphyries.

In the hornblende porphyry, phenocrysts consist of euhedral to subhedral plagioclase (~37·5 vol. %), amphibole (~9·9 vol. %) and magnetite (~1·4 vol. %, with common maghemitization at its rim), with occasional 'book biotite' and K-feldspar. The hornblende–biotite porphyry has more abundant magmatic 'book' biotite (~1·2 vol. %), K-feldspar (~1·2 vol. %), plagioclase (~43·6 vol. %) and a lesser amount of amphibole (~6·1 vol. %). Euhedral, wedge-shaped titanite is very common (up to 0·9 vol. %) in both of these porphyries. Locally, chilled margins of the hornblende–biotite porphyry were found to contain as much as 10 vol. % more groundmass than its more crystalline equivalent and consequently a lesser amount of phenocrysts (except magnetite). The rhyodacite is pervasively altered and amphibole is replaced by chlorite and clay minerals. Magnetite is not preserved and is replaced by hematite. However, it is still possible to estimate the pre-alteration modal mineralogy of this rock, although with a higher uncertainty. The rhyodacite contains more groundmass (~56·2 vol. %) and 'book biotite' (~1·7 vol. %), and less amphibole (~2·8 vol. %) than the other porphyries. Titanite was not observed in this rock. Neither magmatic anhydrite nor sulphides were observed in the unaltered porphyries.

### Plagioclase

Plagioclase phenocrysts in the porphyries are mostly unzoned in backscattered electron (BSE) images and are albite rich (Figs. 8b, 4h–j). Only few crystals display dissolution–recrystallization textures with a slightly more albitic overgrowth compared with the dissolved core (Fig. 8c). However, oscillatory zoning is sometimes observed under the optical microscope (Fig. 8d). Plagioclase composition is very restricted within a single rock type and becomes increasingly albitic from the hornblende porphyry (median ~An20) to the hornblende–biotite porphyry (median ~An15) and the rhyodacite (~An12; Fig. 4h–j). In each porphyry fine spongy cellular rings commonly separate the homogeneous core of plagioclases from their thin overgrowth rims (Fig. 8a–d). In the hornblende porphyry, plagioclase rims are compositionally more diverse (An20-40) than the cores (An18-26; Fig. 4j).

Trace element profiles in plagioclase show very scattered trends in contrast with the relatively homogeneous anorthite composition (Fig. 4h–j). In some grains, La exhibits inverse zoning, sometimes with a relatively abrupt (over < 50 μm) contact between a low-La core and a high-La rim (Fig. 4h and i).

### Hornblende

Amphiboles may lack zoning or may display oscillatory or patchy zoning (Fig. 8e–g). It is common to find zoning-free cores grading out to faint oscillatory zoned rims (Fig. 8e and f). In such cases, both the broad core and the oscillatory-zoned rim may exhibit superimposed patchy zoning.

Amphiboles in the porphyries have slightly lower Mg# [0·60–0·75; Mg# = Mg/(Mg + Fe$^{2+}$)] than those from the gabbrodiorite complex. In the classification scheme of Leake *et al.* (1997), most are magnesio-hornblendes and less commonly edenite [6·5 < Si < 7·5; (Na + K)$_A$ ≥ 0·5; Fig. 5d and e]. A few high-Al$_T$ (>1·8 p.f.u.) crystals plot in the field of magnesio-hastingsite. Slightly altered amphiboles have bleached colors and exhibit composition shifts toward the field of actinolite as a result of Fe depletion and Ca and Si addition. This bleaching mostly corresponds to the patchy zoning observed in BSE images (Fig. 8f and g).

Al$_T$ ranges from 0·8 to 1·7 p.f.u. for the main amphibole population and from 1·8 to 2·4 for the high-Al
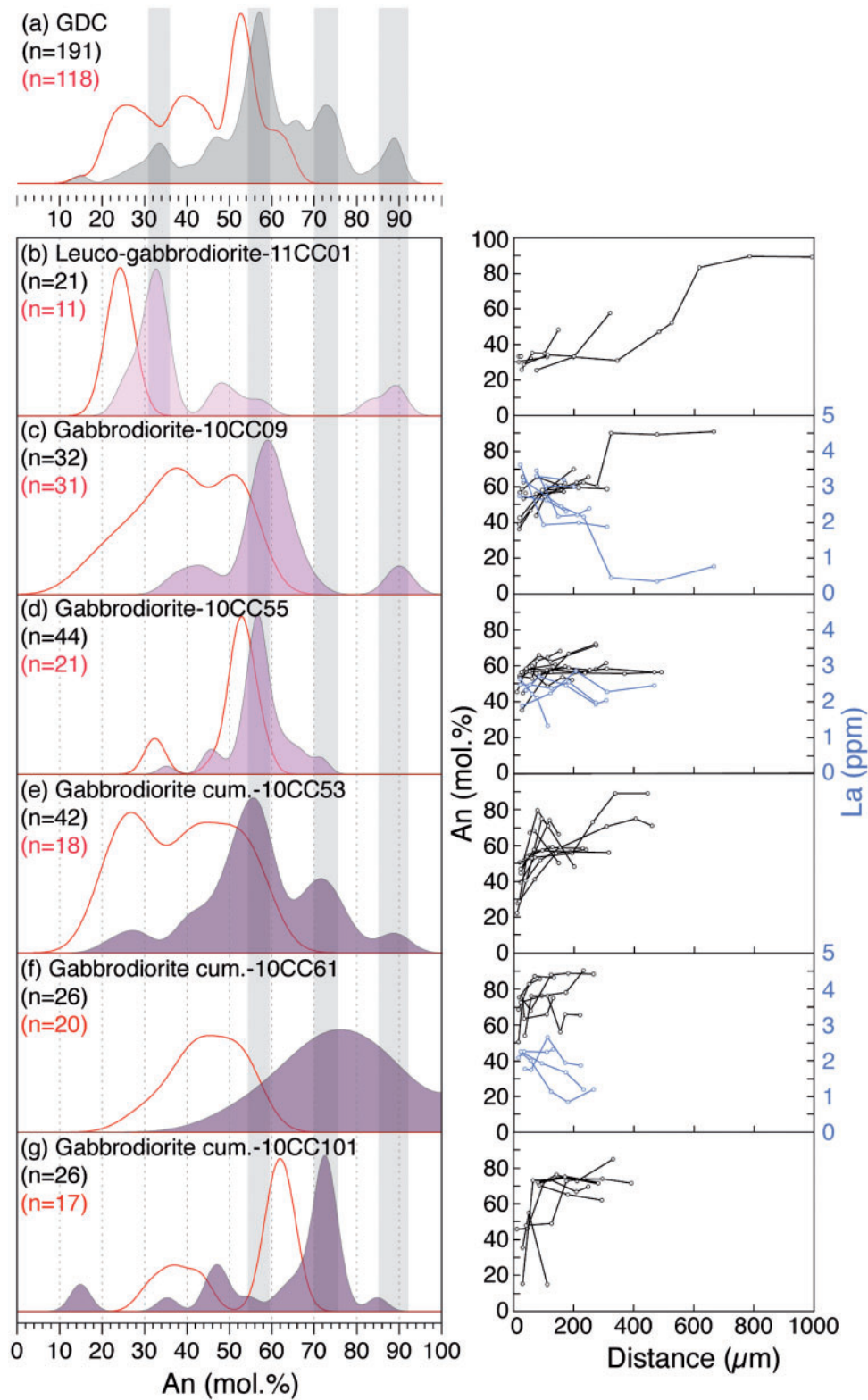
**Fig. 4.** Plagioclase composition in (a–g) the GDC and (h–j) the porphyries. Left column: density distribution of plagioclase anorthite content. Grey shaded bars in samples of the GDC correspond to average plagioclase populations as defined by their anorthite content (see text for discussion). The red curves corresponds to the density distribution of plagioclase anorthite content theoretically in equilibrium with hornblende as calculated using the formulation of Holland & Blundy (1994) using the reaction edenite + albite = richterite + anorthite. *P* and *T* required for the calculation were obtained by the hornblende-only thermobarometric formulation of Ridolfi & Renzulli (2012). In (i) and (j) the continuous line is without Na-correction, short-dashed line is with an Na – 0·1 p.f.u. correction and long-dashed line is with an Na – 0·2 p.f.u. correction (see text for discussion). Right column: rim (distance = 0 µm) to core An and La zoning profiles of plagioclases.
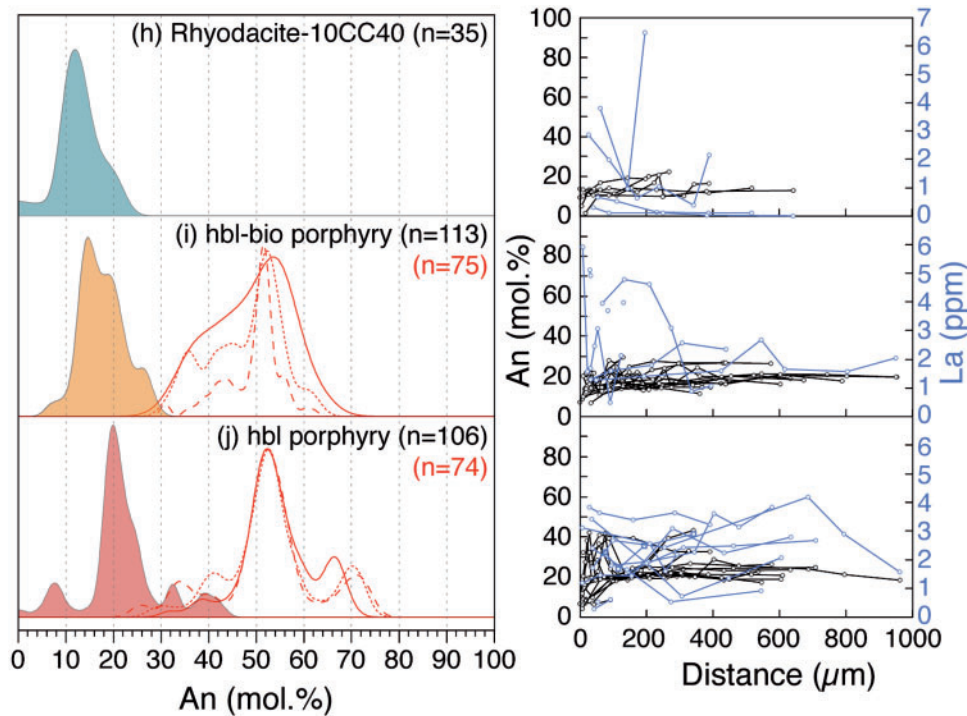
**Fig. 4.** Continued

group. For the main amphibole group, $Al_T$ correlates positively with $(Na + K)_A$ ($r = 0.84$), and shows a poor correlation with $Al_{VI}$ ($r = 0.40$; Fig. 5e and f). For a given $Al_T$, amphiboles from the hornblende–biotite porphyry systematically have $Na_A$ 0·1 p.f.u. higher than amphiboles from the hornblende porphyry (Fig. 5e). No other systematic difference between amphiboles from the two rock types was observed.

Trace element contents of most amphiboles are broadly constant at any given $Al_T$ and are typically more homogeneous that in the GDC (Fig. 6). In the hornblende porphyry, some amphibole cores plot outside the main group and define a high-MREE–HREE–Y–Ta group with a more pronounced negative Eu anomaly ($Eu/Eu^* = 0.5$–$0.6$ versus $0.6$–$0.8$ for the main group of hornblendes) at $Al_T \sim 1.4$ p.f.u. (circled points in Fig. 6g, i and j). The high-Al amphiboles are notably enriched in Sr ($\sim$300 ppm) and Ba ($\sim$150 ppm) and have a high Ba/La ratio ($\sim$40) compared with the main amphibole group (Sr = 50 ppm, Ba = 20–120 ppm, Ba/La = 10). Amphiboles from the porphyries have Sr/Y and $(La/Yb)_N$ values of 1–4, which is higher than amphiboles from the GDC.

### Titanite

Titanite in the hornblende and hornblende–biotite porphyries is euhedral to subhedral and occurs alone or as inclusions in plagioclase, amphibole or biotite. Its internal texture can be variable, but it commonly shows dissolution–overgrowth textures (Fig. 8h). It may contain ilmenite–hematite inclusions sometimes aligned along what could be a growth surface.

### K-feldspar

K-feldspars from the hornblende–biotite porphyry and the rhyodacite are Or60–70. They usually occur as independent phenocrysts, which incorporate earlier formed plagioclase and hornblende (Figs 2 and 8i), but can also overgrow an earlier plagioclase (Fig. 8j). Both types commonly have high Ba contents ranging from 1·6 to 2·8 wt % BaO. Barium displays complex concentric zoning in BSE images (Fig. 8i) with, from core to rim, a smooth BaO decrease in each zone and a sharp BaO increase in the outer rim. K-feldspar overgrown over plagioclase crystals commonly displays a sieve texture similar to the outer rim of K-feldspar phenocrysts (Fig. 8i and j).

## WHOLE-ROCK GEOCHEMISTRY

The Coroccohuayco magmatic suite displays a wide range in composition from $SiO_2 = 48.9$ to 69·6 wt % with a compositional gap from $SiO_2 = 52$ to 62 wt % bridged by only two volumetrically minor leuco-gabbrodiorite samples (Table 2, Fig. 9). This chemical evolution is correlated with age, with the more basic compositions being older (i.e. the GDC at *c.* 40·4 Ma) and the more silicic being younger (i.e. the rhyodacite at *c.* 35·0 Ma). The compositional gap also corresponds to the magmatic lull evidenced by radiometric dating (Chelle-Michou *et al.*, 2014) from 40·2 to 35·6 Ma. Overall, the magmatic suite falls within the calc-alkaline field and extends into the high-K calc-alkaline field (Fig. 9g). $TiO_2$, $Fe_2O_{3[Tot]}$, MgO, MnO, CaO and the high field strength elements (HFSE) display negative correlations with $SiO_2$, whereas
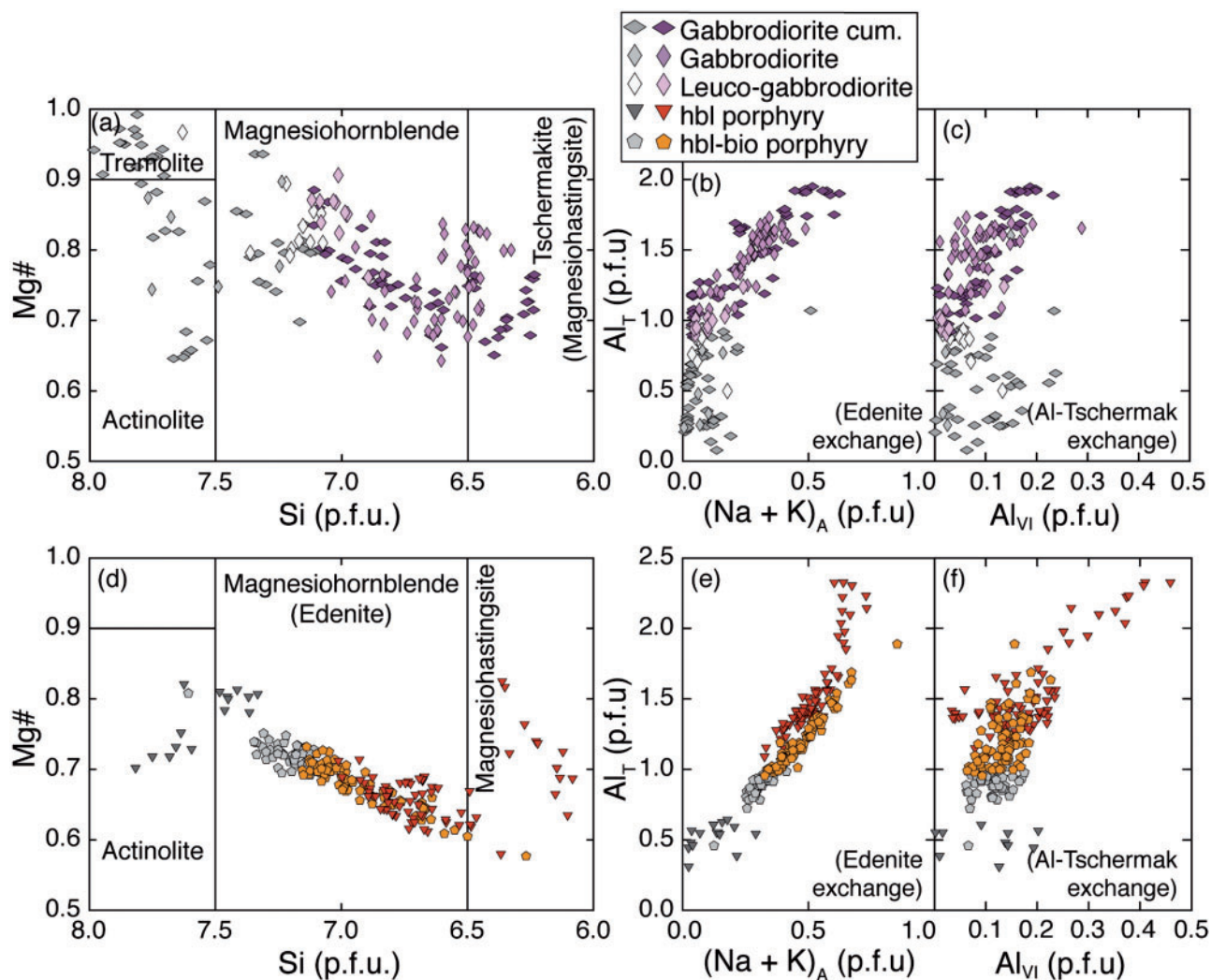
**Fig. 5.** Amphibole compositions illustrating (a, d) their classification and (b, c, e, f) substitution mechanisms. Colored symbols indicate amphiboles that match the compositional calibration range of the thermobarometric formulations of Ridolfi & Renzulli (2012). Greyscale symbols correspond to amphiboles that plot outside this compositional range, many of which show clear signs of hydrothermal alteration.

$K_2O$ and $NaO$ show a positive correlation (Fig. 9a–e, g and h). $Al_2O_3$ contents are generally high and range from ~19 wt % for the GDC to ~17 wt % for the porphyries (Fig 9f). With increasing $SiO_2$ content $P_2O_5$, Ta and Y contents increase in the GDC and decrease in the porphyries (Fig. 9i, k and l). Zr, Sr and Th are positively correlated with $SiO_2$ but are depleted in the rhyodacite compared with the other porphyries (Fig. 9j, m and n). Over time the magmatic suite exhibits an increase in Sr/Y (c. 20–130) and Zr/Y (c. 2–15) from the gabbrodiorite to the rhyodacite (Fig. 10c and d).

Compared with primitive mantle compositions all the magmatic rocks at Coroccohuayco display prominent negative Nb and Ta anomalies and an enrichment of large ion lithophile elements (LILE) over HFSE, typical of arc magmas (Fig. 10b); Pb and Sr exhibit positive anomalies. Samples from the GDC are slightly enriched in LREE over HREE. Gabbrodiorite and leuco-gabbrodiorite samples display a range of overlapping chondrite-normalized REE patterns and no Eu anomalies (Fig. 10a). The $P_2O_5$, Zr and REE + Y contents of the gabbrodiorite 'cumulate' are typically characterized by lower values (by 30–50%) but similar ratios (e.g. La/Yb, Zr/Y) and a positive Eu anomaly (Figs 9i, j, l and 10). Compared with the GDC, the porphyries are more enriched in LILE and LREE, and depleted in HFSE and HREE (Fig. 10b). They show slightly more significant negative Eu and Ti anomalies. REE patterns display a listric shape for all the porphyries, and total REE content decreases from the hornblende porphyry to the rhyodacite (Fig. 10a).

Isotopic compositions of Sr and Nd are variable for samples of the GDC but are relatively well correlated for the porphyries (Fig. 11a). The GDC yields higher $\varepsilon Nd_{36\ Ma}$ values (+2·6 to +0·9) than the porphyries (+0·3 to –1·3) but similar $^{87}Sr/^{86}Sr_{36\ Ma}$ values (0·7048–0·7057). In a Sr vs Nd isotope plot, there is a clear temporal trend toward increasingly crustal isotopic composition from
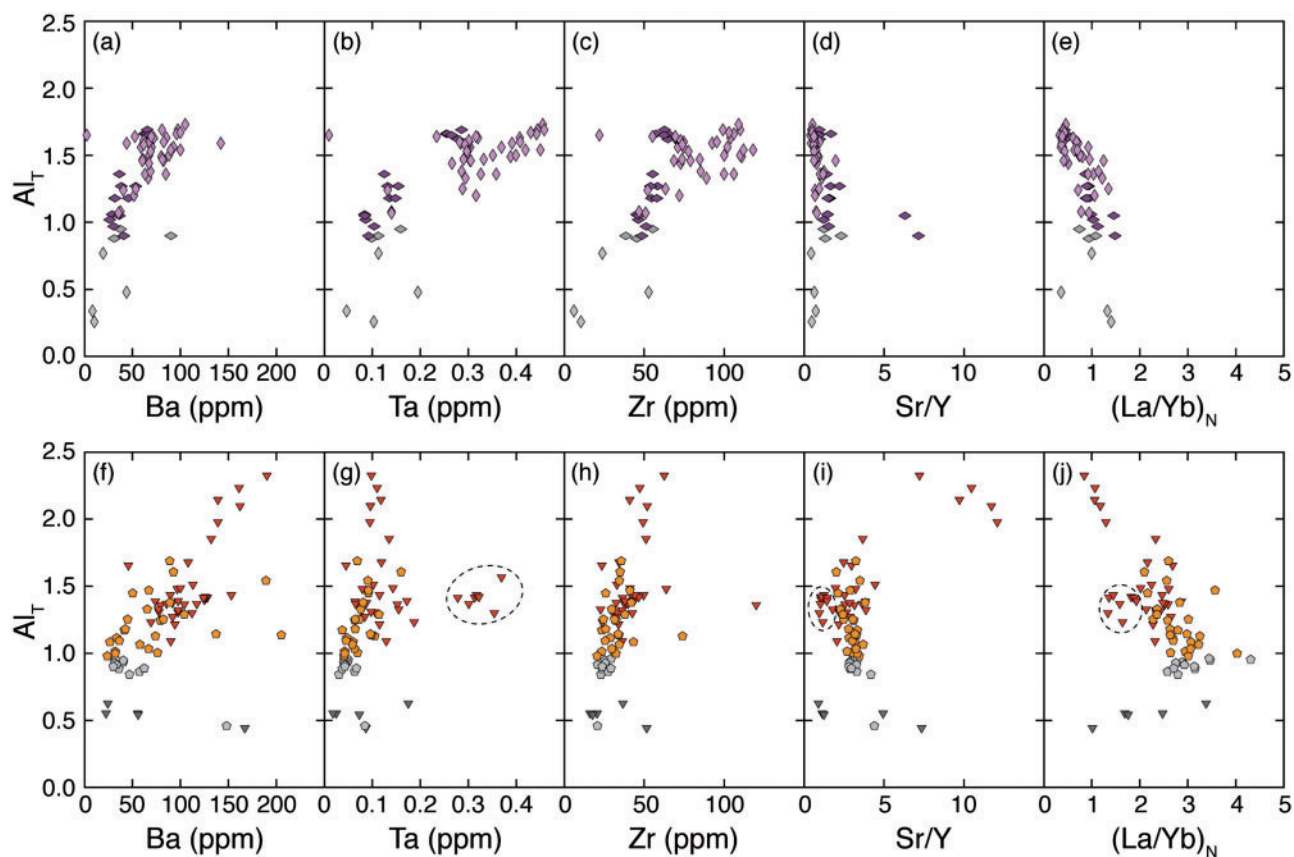
**Fig. 6.** Trace element composition of amphiboles. (a, f) Ba, (b, g) Ta, (c, h) Zr, (d, i) Sr/Y, and (e, j) (La/Yb)$_N$ vs Al$_T$. The two groups of amphiboles best defined in the Zr plots for a given Al$_T$ in samples of the gabbrodiorite should be noted; also the high Ta content and low (La/Yb)$_N$ of some amphiboles in the hornblende-porphyry [circled points in (g and j)]. These hornblendes also have high REE contents (see text for discussion). Legend is the same as in Fig. 5.

the GDC to the rhyodacite (Fig. 11a). The Pb isotopic values of the gabbrodiorite complex and the porphyries, corrected for U and Th decay, overlap ($^{206}$Pb/$^{204}$Pb = 18·35–18·62, $^{207}$Pb/$^{204}$Pb = 15·58–15·64, $^{208}$Pb/$^{204}$Pb = 38·37–38·61; SD Table 5); the porphyries have more radiogenic present-day values compared with the GDC (Fig. 11b). All the magmatic rocks at Coroccohuayco have transitional values between the Paracas Paleozoic basement block and the Arequipa basement block (Fig. 11b), consistent with the geographical location of the Tintaya District at the border between the two blocks (see Mamani *et al.*, 2010).

## INTENSIVE PARAMETERS OF MAGMA EVOLUTION (*P–T–* H$_2$O–*f*O$_2$)

To determine intensive parameters for the magmas (pressure, temperature, melt H$_2$O concentration and oxygen fugacity) we used the empirical formulation of Ridolfi & Renzulli (2012). This formulation has the advantage of being based on amphibole-only compositions, provided that their chemistry matches those of the amphiboles used for the calibration and that they grow in equilibrium with their parent melt. However, despite these obvious advantages, much debate

surrounds the accuracy of the calculated intensive variables (e.g. Walker *et al.*, 2013; Erdmann *et al.*, 2014). Therefore, we also indirectly compare the pressure and temperature outputs of this empirical formulation with the hornblende–plagioclase thermodynamic formulation of Holland & Blundy (1994; based on the reaction edenite + albite = richterite + anorthite). Plagioclase–hornblende equilibrium (necessary for the application of Holland & Blundy's formulation) can be difficult to evaluate on a thin section scale. Therefore, we have calculated the composition of plagioclase that would theoretically be in equilibrium with amphibole at the pressure and temperature values calculated using the formulation of Ridolfi & Renzulli (2012), leaving the plagioclase anorthite composition as the only unknown variable. This calculated plagioclase composition is subsequently compared with the analysed one.

### Application of empirical calibrations for amphibole

The determination of intensive parameters has been conducted on amphiboles that match the compositional field used for the calibration of the equations (coloured symbols in Figs 5, 6 and 12; Ridolfi & Renzulli, 2012).
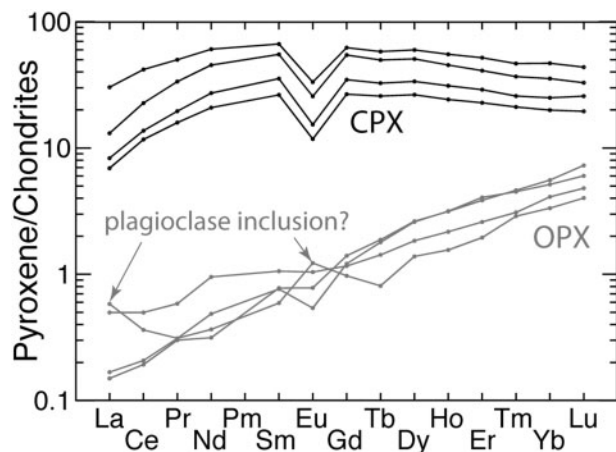
**Fig. 7.** Clinopyroxene and orthopyroxene chondrite-normalized REE patterns [normalizing values from McDonough & Sun (1995)].

Amphiboles from both the GDC and the porphyries yield very similar *P*, *T* and $H_2O_{melt}$ values (Fig. 12). Profiles within single crystals often result in variable *P* (and *T* to a lesser extent), by as much as ~200 MPa, with no systematic changes from core to rim. These apparent magmatic condition changes are unrealistic and may result from the kinetics of amphibole growth where amphibole chemistry is not at equilibrium with the melt (Costa *et al.*, 2013). A more limited range of pressure is also supported by a lack of significant pressure-sensitive substitutions (e.g. Al-Tschermak; Fig. 5c and f). However, clear evidence for edenite exchange (Fig. 5b and e) supports the temperature-controlled compositional variability of the hornblendes. Therefore, we argue that, with the exception of some anomalous values, our large dataset (~400 points) captures the main features of the magmatic conditions at Coroccohuayco.

The main amphibole population (for both the GDC and the porphyries) yields pressures between 250 and 100 MPa (median at 147 MPa), temperatures from 900 to 750°C (median at 833°C) and $H_2O_{melt}$ around $5 \pm 1$ wt % (Fig. 12). For the high-Al amphiboles in the hornblende porphyry, calculated pressures vary from 1600 to 1200 MPa, temperatures range from 1100 to 960°C and the melt water content is around 11 wt %.

The $fO_2$ determinations from amphiboles of the GDC yield values of $\Delta NNO \pm 1$ (where NNO is the nickel–nickel oxide oxygen buffer, Fig. 12c). In contrast, amphiboles from the porphyries give a higher $fO_2$ from $NNO + 1.5$ to $NNO + 3$. At a given pressure, values from the hornblende–biotite porphyry are systematically ~0·5 log unit higher than those from the hornblende porphyry (Fig. 12f). High-Al amphiboles give high $fO_2$ around $NNO + 3.5$.

## Plagioclase composition theoretically in equilibrium with hornblende

For the GDC, our calculations show that amphiboles should be in equilibrium with slightly more sodic plagioclase than the majority of that observed in these samples (Fig. 4a–g). In most cases this corresponds to the actual composition of plagioclase rims. This is consistent with the observation that amphibole crystals are oikocrysts that grew incorporating previously formed euhedral plagioclase. Interestingly, for most samples of the GDC, our calculations show the presence of two plagioclase populations that are in equilibrium with the distinct amphibole populations found in these samples (Fig. 4c–e and g).

Assuming that *P* and *T* were correctly estimated for the porphyries, the plagioclase composition in equilibrium with amphibole should be ~An30–70 (Fig. 4h–j). Such compositions are rarely found in the porphyries at Coroccohuayco. However, the albitic compositions observed in plagioclase from the porphyries are not common for water-rich magmas (e.g. Lange *et al.*, 2009). Considering a plagioclase composition of ~20% An (i.e. the composition of most plagioclases in the hornblende porphyry), we also calculated *P* and *T* using the thermobarometric formulation of Holland & Blundy (1994) in conjunction with the Al-in-hornblende barometer of Anderson & Smith (1995) to allow for simultaneous determination of *P* and *T* (see Anderson *et al.*, 2008). We obtained a range of *P* and *T* of 400–100 MPa and 750–650°C, respectively. Although this pressure range seems reasonable, such a low temperature range (around the water-saturated granitic solidus) is unlikely to represent the crystallization temperature of all the amphiboles in the porphyries. This analysis shows that, in the porphyries, plagioclase and hornblende are no longer in magmatic equilibrium, which prevents the use of thermodynamically based thermobarometers for these rocks.

We conclude that for both the GDC and the porphyries, intensive parameters estimated with the calibrations of Ridolfi & Renzulli (2012) overall provide reasonable estimates for the Coroccohuayco magmatic suite.

## Influence of post-crystallization Na addition in amphibole on calculated intensive parameters for the porphyries

Several lines of evidence suggest that sodium was added to plagioclase and amphibole after the porphyries crystallized: (1) plagioclase found in these rocks essentially lacks anorthite zoning, is significantly more albitic than plagioclase theoretically in equilibrium with amphibole, and displays zoning of La that is not correlated with plagioclase composition in contrast to plagioclase from the GDC (Fig. 4); (2) the three porphyries exhibit high $Na_2O$ content (5–6 wt %), above the compositional range of magmatic rocks of the Eocene Anta arc (Fig. 9h); (3) within a single rock type, plagioclase composition is relatively homogeneous and becomes increasingly albitic from the hornblende porphyry to the hornblende–biotite porphyry and the rhyodacite (Fig. 4h–j); (4) for a given amphibole $Al_T$, $Na_A$ is systematically ~0·1 p.f.u. higher in the hornblende–biotite
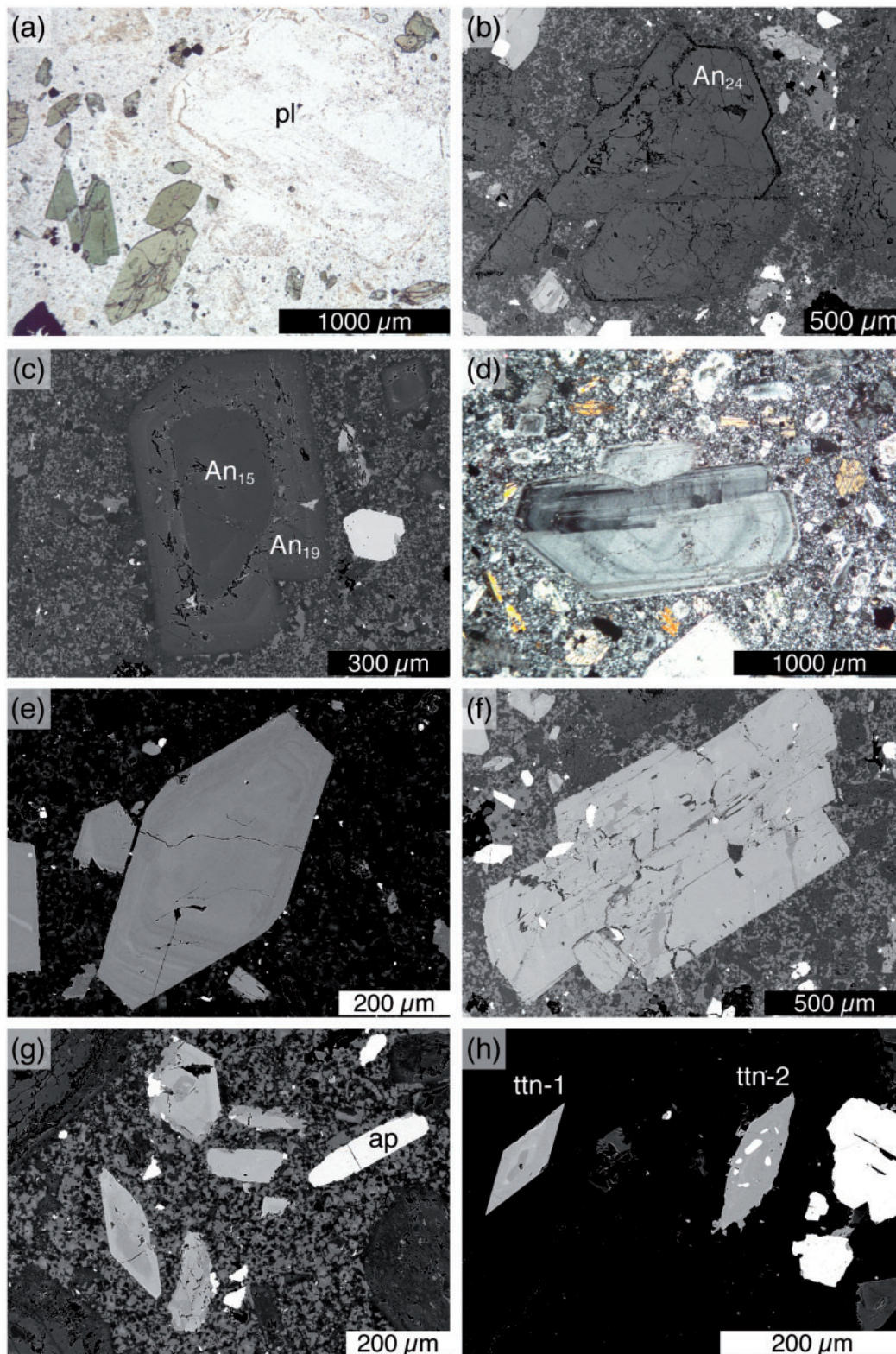
**Fig. 8.** Photomicrographs of samples from the porphyries. (a) Amphibole and plagioclase phenocrysts (plane-polarized light). The irregular spongy cellular ring in the plagioclase should be noted. (b) Plagioclase aggregate with weak zoning (BSE image). (c) Zoned plagioclase with dissolution texture and overgrowth of a slightly less albitic rim (BSE image). (d) Oscillatory zoning plagioclase with spongy cellular ring between core and rim (cross-polarized light). This type of zoning is never observed in BSE images. (e, f) Amphiboles with broad core and fine oscillatory zoning toward the rim (BSE images). (g) Zoned high-Al amphiboles; darker zones represent actinolite alteration (BSE image). (h) Titanite (BSE image). ttn-1 has a dissolution–overgrowth texture; ttn-2 has ilmenite–hematite drop-like inclusions. (i) Zoned K-feldspar phenocryst in the hornblende–biotite porphyry (BSE image). Microprobe analyses of Ba (white circles, spot location; orange circles, BaO content) illustrate this zoning. (j) Plagioclase with K-feldspar overgrowth (BSE image). An, plagioclase anorthite content; ap, apatite; pl, plagioclase; ttn, titanite;.
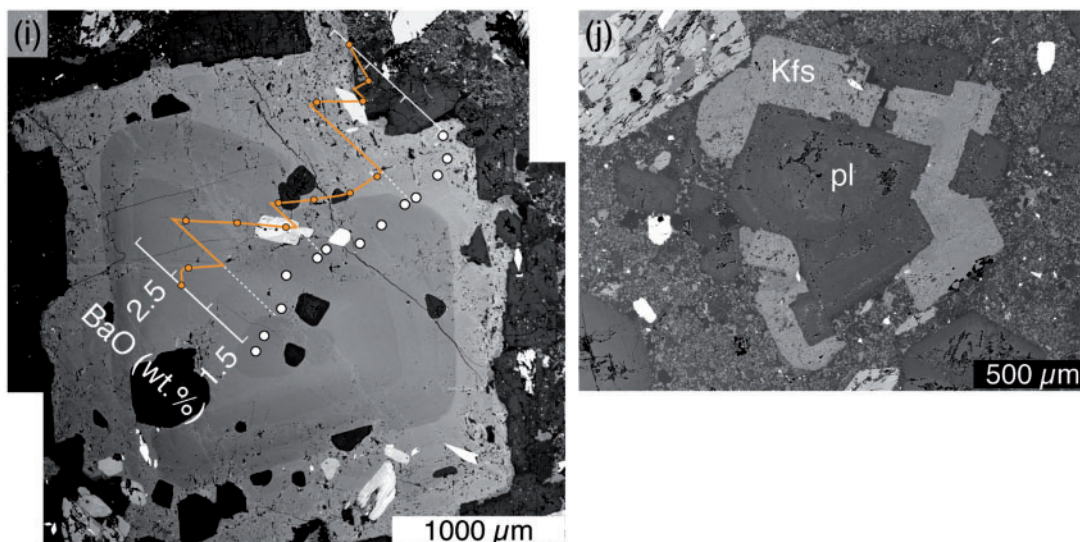
**Fig. 8.** Continued

porphyry relative to the hornblende porphyry (Fig. 5e). This Na addition could result from high-temperature sodic alteration that is well documented in porphyry systems (e.g. Seedorff *et al.*, 2005, 2008) and has been shown experimentally to occur rapidly on short time-scales (Hövelmann *et al.*, 2010). However, such alteration usually results in dusty and porous plagioclase (Engvik *et al.*, 2008; Plümper & Putnis, 2009; Hövelmann *et al.*, 2010) and in albite rims around magmatic K-feldspar (Norberg *et al.*, 2011), which are not observed at Coroccohuayco. Instead, the optical zoning of plagioclase appears to be preserved (Fig. 8d).

Regardless of the actual process responsible for this Na addition, the impact of post-crystallization incorporation of Na in the A site of the amphibole on the determination of the intensive parameters need to be evaluated. We have recalculated the intensive parameters by artificially decreasing $Na_A$ by 0·1 p.f.u ($\sim$0·35 wt % $Na_2O$) and 0·2 p.f.u. ($\sim$0·70 wt % $Na_2O$; Fig. 13) for all amphiboles from the porphyries. Subtracting 0·2 p.f.u Na corresponds to removing all $Na_A$ from the low-Al amphiboles, and is therefore considered to be a maximum correction. For the main amphibole population, pressure is found to change relatively by –6 $\pm$ 14% and –4 $\pm$ 15% (1SD) when removing 0·1 and 0·2 p.f.u. Na, respectively. For high-Al amphiboles, the effect of the Na-correction is much larger with –47% and –64% for Na – 0·1 and Na – 0·2, respectively. For the main group of low-Al amphiboles, the Na-correction tends to reduce the scatter in the calculated pressure (Fig. 13a). For temperature, Na-corrections yield values 2·7 $\pm$ 0·4% and 5·1 $\pm$ 0·5% lower than without correction. At 800°C, this corresponds to a temperature decrease of 22°C and 41°C, respectively (Fig. 13b). Melt water content calculated with Na-correction is mostly within the model uncertainty of $\pm$0·78 wt % $H_2O$ (Fig. 13c; Ridolfi & Renzulli, 2012). Only for the high-Al amphiboles do Na-corrections yield water contents 2·1 wt % and 3·0 wt % lower

than those without correction. Na-corrections induce the most significant changes on the determination of the oxygen fugacity. Reduction of Na of 0·1 p.f.u and 0·2 p.f.u yields oxygen fugacities lower by 0·6 log unit and 1·2 log units, respectively (Fig. 13d). Importantly, it shows that even applying Na-corrections to the data, the oxygen fugacity of the porphyry is $\sim$NNO + 1, which is higher than the average oxygen fugacity of the gabbrodiorite complex (Figs 12c, f and 13d). Finally, the effect of these corrections on the calculation of the plagioclase composition theoretically in equilibrium with amphibole is negligible (Fig. 4h–j).

## Influence of the presence of S in the magma on calculated intensive parameters for the porphyries

The equations of Ridolfi & Renzulli (2012) were calibrated with data from a set of S-free experiments. However, the genetic link between the porphyries and the mineralization suggests that the magmatic system may have been S-rich at the time of porphyry emplacement. The presence of S in a water-saturated dacitic magma has been experimentally shown to increase the Mg# [calculated as Mg/(Mg + Fe)] of amphibole by up to 0·1 for oxygen fugacities in the field of sulfide stability (<NNO + 1; Scaillet & Evans, 1999). In contrast, no significant difference in amphibole chemistry for S-free and S-bearing experiments was detected above NNO + 1·5 (Scaillet & Evans 1999; Costa *et al.*, 2004). Compared with the gabbrodiorite complex, the presence of titanite relative to ilmenite in the porphyries (Wones, 1989; Nakada, 1991; Xirouchakis & Lindsley, 1998; Frost *et al.*, 2001; McLeod *et al.*, 2011) and the higher Ce/Nd in zircon from the porphyries (used as a proxy for the zircon Ce anomaly and magma oxidation state; Chelle-Michou *et al.*, 2014) suggest that the oxygen fugacity of the porphyries is higher than that of the GDC; that is, above NNO + 1. Consequently, the likely

**Table 2**: Representative geochemical and isotopic data for the Coroccohuayco magmatic suite

| Rock type: | Gabbrodiorite 'cumulate' | Gabbrodiorite | | Leuco-gabbrodiorite | Hornblende porphyry | Hornblende–biotiteporphyry | Rhyodacite |
|---|---|---|---|---|---|---|---|
| Sample no.: | 10CC61 | 10CC09 | 10CC55 | 10CC16 | 10CC22 | 10CC94 | 10CC40 |
| Sample type: | Outcrop | Outcrop | Outcrop | Outcrop | Outcrop | Drillcore | Outcrop |
| Coord E/DDH#: | 256574 | 256706 | 256812 | 256546 | 257328 | A400-19·9 | 257497 |
| Coord N/depth: | 8344662 | 8346226 | 8345420 | 8345406 | 8344904 | 31·7 m | 8345019 |
| *Major elements (wt %)* | | | | | | | |
| $SiO_2$ | 47·26 | 52·09 | 49·15 | 54·83 | 63·18 | 65·56 | 69·60 |
| $TiO_2$ | 0·96 | 0·93 | 1·00 | 0·68 | 0·54 | 0·36 | 0·21 |
| $Al_2O_3$ | 19·58 | 17·76 | 19·09 | 19·26 | 16·94 | 17·17 | 17·17 |
| $Fe_2O_3$ (tot) | 12·17 | 10·34 | 11·43 | 6·06 | 4·50 | 2·87 | 1·69 |
| MnO | 0·21 | 0·16 | 0·16 | 0·08 | 0·04 | 0·03 | 0·03 |
| MgO | 5·25 | 4·49 | 4·18 | 3·55 | 1·60 | 0·85 | 0·36 |
| CaO | 11·49 | 8·96 | 9·63 | 9·08 | 3·52 | 2·83 | 1·00 |
| $Na_2O$ | 1·75 | 2·74 | 3·12 | 4·46 | 5·39 | 5·95 | 5·68 |
| $K_2O$ | 0·28 | 0·77 | 0·70 | 0·63 | 2·73 | 2·63 | 2·88 |
| $P_2O_5$ | 0·12 | 0·11 | 0·20 | 0·18 | 0·21 | 0·14 | 0·08 |
| LOI | 0·43 | 0·70 | 0·54 | 0·45 | 0·53 | 1·37 | 1·09 |
| Total | 99·50 | 99·05 | 99·19 | 99·26 | 99·17 | 99·75 | 99·80 |
| Mg# | 0·46 | 0·46 | 0·42 | 0·54 | 0·41 | 0·37 | 0·30 |
| *Trace elements (ppm)* | | | | | | | |
| Sr | 429 | 345 | 428 | 416 | 794 | 877 | 612 |
| Ga | 19 | 19 | 21 | 19 | 20 | 21 | 21 |
| Cu | 72 | 43 | 304 | 21 | 361 | 5 | 6 |
| Cr | 14 | 11 | 12 | 11 | 16 | 8 | 6 |
| Ba | 77 | 226 | 168 | 236 | 1029 | 1172 | 2339 |
| Sc | 31·43 | 39·91 | 33·70 | 26·10 | 11·26 | 6·49 | 3·00 |
| V | 335 | 351 | 283 | 209 | 130 | 86 | 50 |
| Co | 37·3 | 29·9 | 27·0 | 12·5 | 11·3 | 5·3 | 2·4 |
| Ni | 15·1 | 7·7 | 16·3 | 11·1 | 9·3 | n.d. | 5·5 |
| Zn | 73·2 | 52·4 | 41·3 | 21·8 | 16·4 | 24·0 | 193·1 |
| As | 0·90 | 0·86 | 0·98 | 0·96 | 0·69 | 1·31 | 1·20 |
| Rb | 6·8 | 21·1 | 15·0 | 8·6 | 41·1 | 56·6 | 75·4 |
| Y | 11·81 | 19·81 | 17·84 | 17·71 | 15·46 | 9·27 | 6·13 |
| Zr | 26·7 | 75·9 | 44·9 | 33·5 | 121·3 | 134·3 | 101·6 |
| Nb | 0·98 | 2·45 | 1·58 | 1·72 | 4·93 | 4·18 | 3·04 |
| Mo | 0·91 | 0·32 | 0·31 | 0·21 | 0·63 | 0·26 | 0·72 |
| Sb | n.d. | 0·22 | 0·09 | 0·23 | 0·23 | 0·21 | 0·24 |
| Cs | 0·26 | 0·80 | 0·17 | 0·36 | 0·15 | 0·67 | 1·80 |
| La | 4·09 | 7·55 | 6·27 | 7·42 | 16·91 | 14·28 | 6·20 |
| Ce | 9·80 | 17·93 | 15·08 | 15·53 | 34·23 | 29·10 | 10·18 |
| Pr | 1·35 | 2·39 | 2·08 | 2·30 | 4·25 | 3·46 | 1·65 |
| Nd | 6·64 | 11·19 | 10·40 | 10·72 | 17·63 | 13·88 | 6·79 |
| Sm | 1·86 | 2·96 | 2·74 | 3·00 | 3·51 | 2·76 | 1·37 |
| Eu | 0·74 | 1·02 | 0·96 | 1·08 | 0·85 | 0·60 | 0·31 |
| Gd | 2·15 | 3·43 | 3·38 | 3·20 | 3·07 | 2·07 | 1·31 |
| Tb | 0·327 | 0·520 | 0·502 | 0·548 | 0·436 | 0·296 | 0·189 |
| Dy | 2·33 | 3·81 | 3·34 | 3·56 | 2·89 | 1·54 | 1·13 |
| Ho | 0·431 | 0·726 | 0·693 | 0·725 | 0·546 | 0·310 | 0·223 |
| Er | 1·30 | 1·94 | 1·76 | 1·89 | 1·60 | 0·91 | 0·63 |
| Tm | 0·177 | 0·324 | 0·257 | 0·275 | 0·247 | 0·147 | 0·101 |
| Yb | 1·23 | 2·09 | 1·80 | 1·80 | 1·58 | 0·95 | 0·73 |
| Lu | 0·169 | 0·317 | 0·269 | 0·245 | 0·264 | 0·177 | 0·106 |
| Hf | 0·94 | 2·10 | 1·34 | 1·06 | 3·30 | 4·03 | 3·12 |
| Ta | 0·072 | 0·149 | 0·096 | 0·108 | 0·309 | 0·260 | 0·191 |
| W | 0·12 | 27·33 | 0·46 | 0·16 | 0·67 | 1·83 | 0·71 |
| Pb | 2·7 | 3·3 | 2·0 | 2·2 | 2·5 | 4·3 | 12·4 |
| Th | 0·56 | 1·52 | 0·79 | 0·64 | 4·60 | 4·74 | 2·02 |
| U | 0·200 | 0·550 | 0·265 | 0·170 | 1·549 | 1·697 | 1·204 |
| *Measured isotopic ratios* | | | | | | | |
| $^{87}Sr/^{86}Sr$ | 0·7048528 | 0·7051751 | 0·7052239 | 0·7053211 | 0·7054340 | 0·7055095 | 0·7056774 |
| $^{143}Nd/^{144}Nd$ | 0·5127635 | 0·5127206 | 0·5127070 | 0·5126710 | 0·5126206 | 0·5126017 | 0·5125519 |
| $^{206}Pb/^{204}Pb$ | 18·533 | 18·551 | 18·569 | 18·536 | 18·817 | 18·725 | 18·647 |
| $^{207}Pb/^{204}Pb$ | 15·616 | 15·616 | 15·625 | 15·626 | 15·651 | 15·639 | 15·635 |
| $^{208}Pb/^{204}Pb$ | 38·478 | 38·506 | 38·522 | 38·509 | 38·825 | 38·693 | 38·599 |
| *Initial isotopic ratios* | | | | | | | |
| $^{87}Sr/^{86}Sr_i$ | 0·7048265 | 0·7050736 | 0·7051728 | 0·7052909 | 0·7053583 | 0·7054151 | 0·7054973 |
| $^{143}Nd/^{144}Nd_i$ | 0·5127182 | 0·5126779 | 0·5126701 | 0·5126318 | 0·5125924 | 0·5125735 | 0·5125235 |
| $\varepsilon Nd_i$ | 2·594 | 1·807 | 1·655 | 0·908 | 0·139 | −0·228 | −1·340 |
| $^{206}Pb/^{204}Pb_i$ | 18·504 | 18·484 | 18·430 | 18·509 | 18·597 | 18·585 | 18·613 |
| $^{207}Pb/^{204}Pb_i$ | 15·614 | 15·613 | 15·618 | 15·624 | 15·640 | 15·632 | 15·634 |
| $^{208}Pb/^{204}Pb_i$ | 38·451 | 38·446 | 38·507 | 38·476 | 38·610 | 38·564 | 38·580 |

DDH#, drillcore number. LOI, loss on ignition; n.d., not detected.
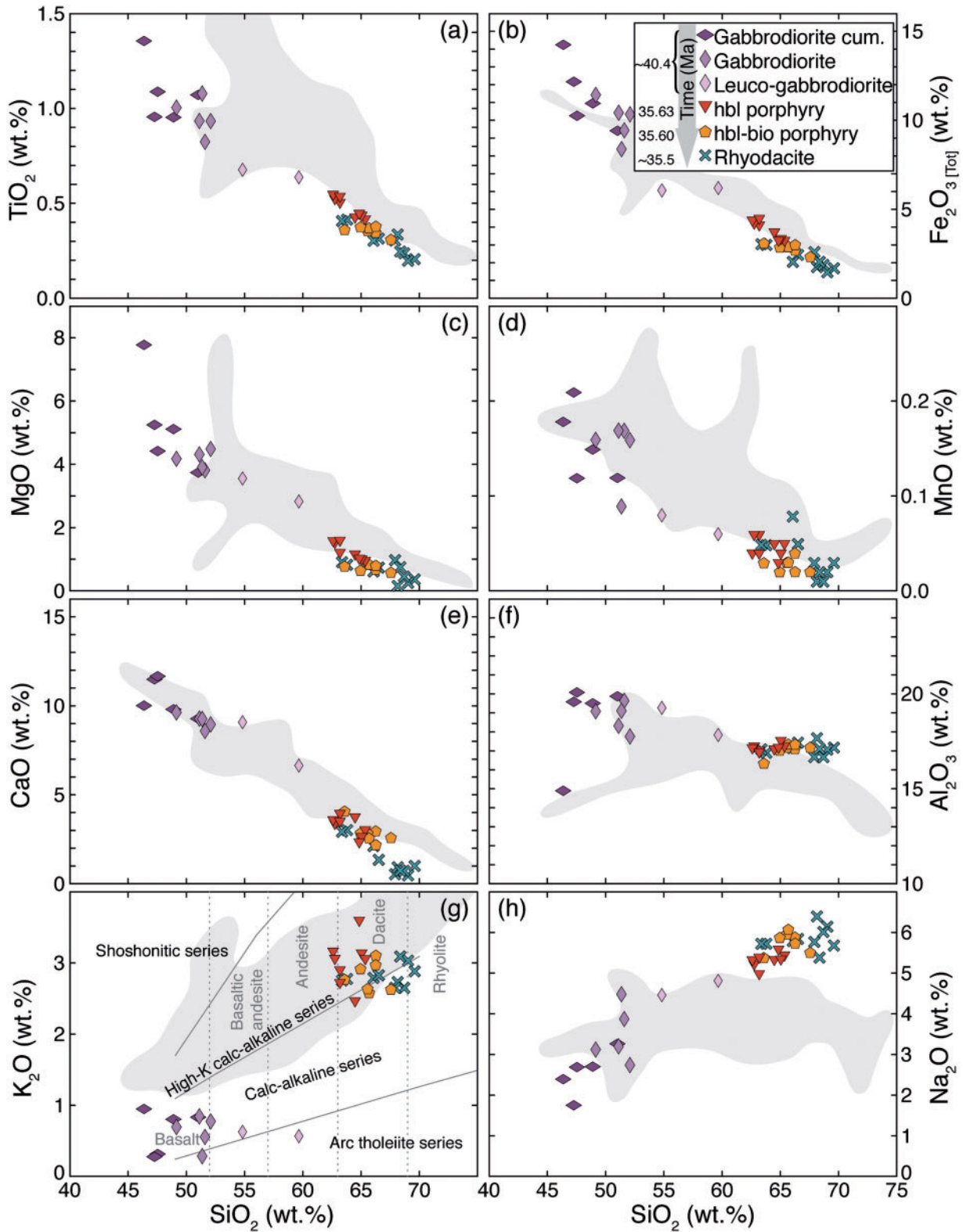
**Fig. 9.** Harker variation diagrams for whole-rock samples of the Coroccohuayco magmatic suite. Grey field delineates the compositional range of magmatic rocks of the Eocene Anta arc (mostly from northern Chile) as compiled by Mamani *et al*. (2010).

presence of S in the melt would not have significantly affected the Mg# of amphiboles from the porphyries, and no influence on the calculation of intensive parameters can be expected.

## PETROLOGICAL EVOLUTION

Our main focus is to constrain the deep and upper crustal processes responsible for the 5 Myr petrological
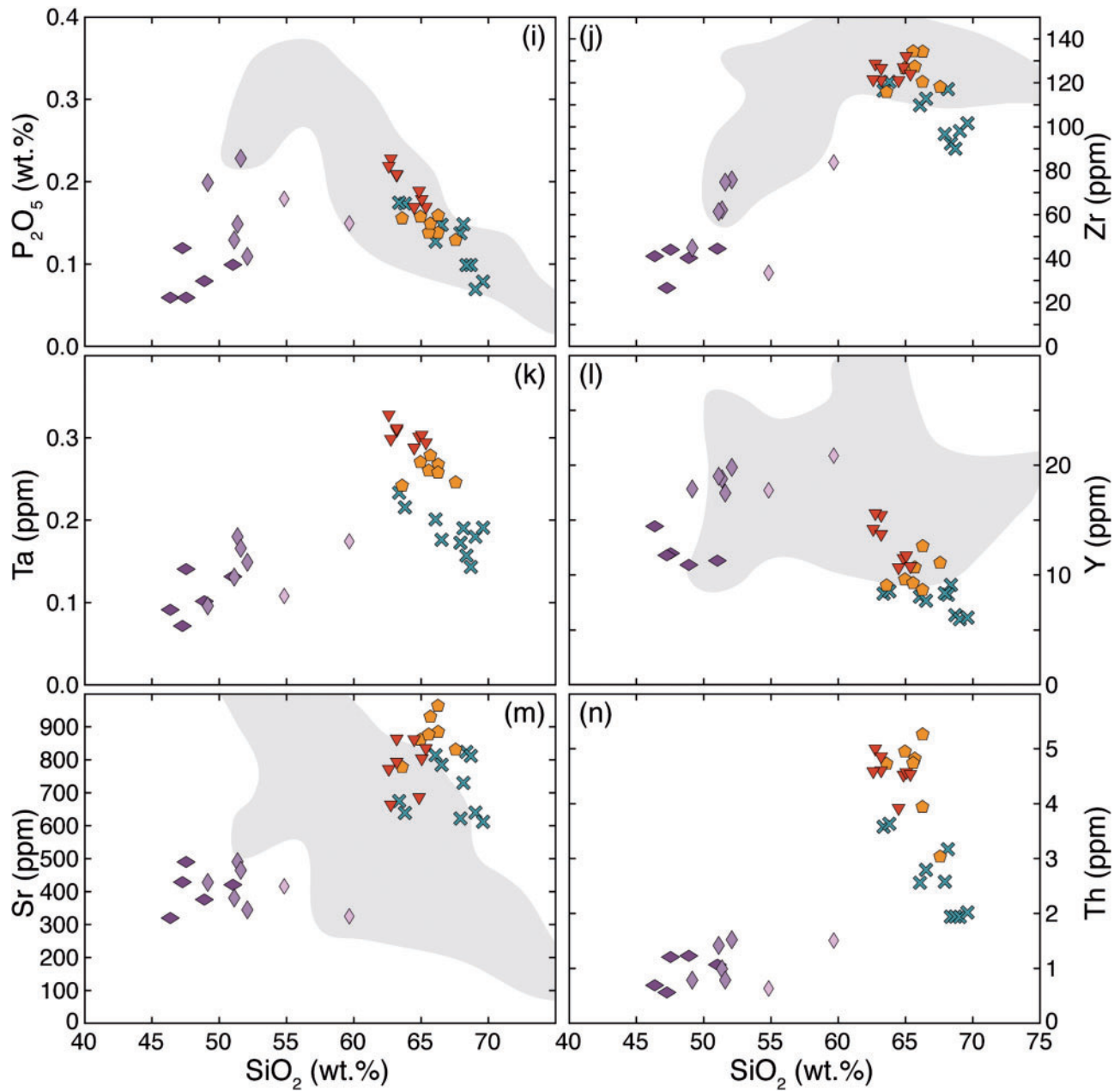
**Fig. 9.** Continued

evolution of the Coroccohuayco magmatic system leading to mineralization. Below, we discuss all the Coroccohuayco magmatic suite evolutionary stages from the magma source to deep crustal and upper crustal evolution from the inception of the magmatic activity (the GDC) to its end (the rhyodacite).

## Magma source

All the magmatic rocks at Coroccohuayco display the strong negative Nb, Ta and Ti anomalies and LILE enrichment that are typical of subduction-related magmas (Fig. 10b). The overlapping Pb isotopic values corrected for U, Th and Rb decay for the GDC and the

porphyries also suggest that they have a similar source (Fig. 11). The most primitive samples of the magmatic suite (the gabbrodiorite samples, $SiO_2 \sim 50$ wt %) have high Ba/La ($\sim$20–30) and Pb/Ce (0·1–0·2), which is diagnostic of the contribution of fluids that have promoted melting of the mantle wedge. In line with established models about subduction-related magmatism, these fluids are likely to have originated by dehydration of the subducting slab (e.g. Tatsumi *et al.*, 1986; Tatsumi, 1989) or of a mélange diapir (e.g. Marschall & Schumacher, 2012). The low Th/La ($<$0·2) and Th/Nb ($<$1) ratios of the GDC suggest minimal involvement of subducted sediment recycling (e.g. Plank, 2005).
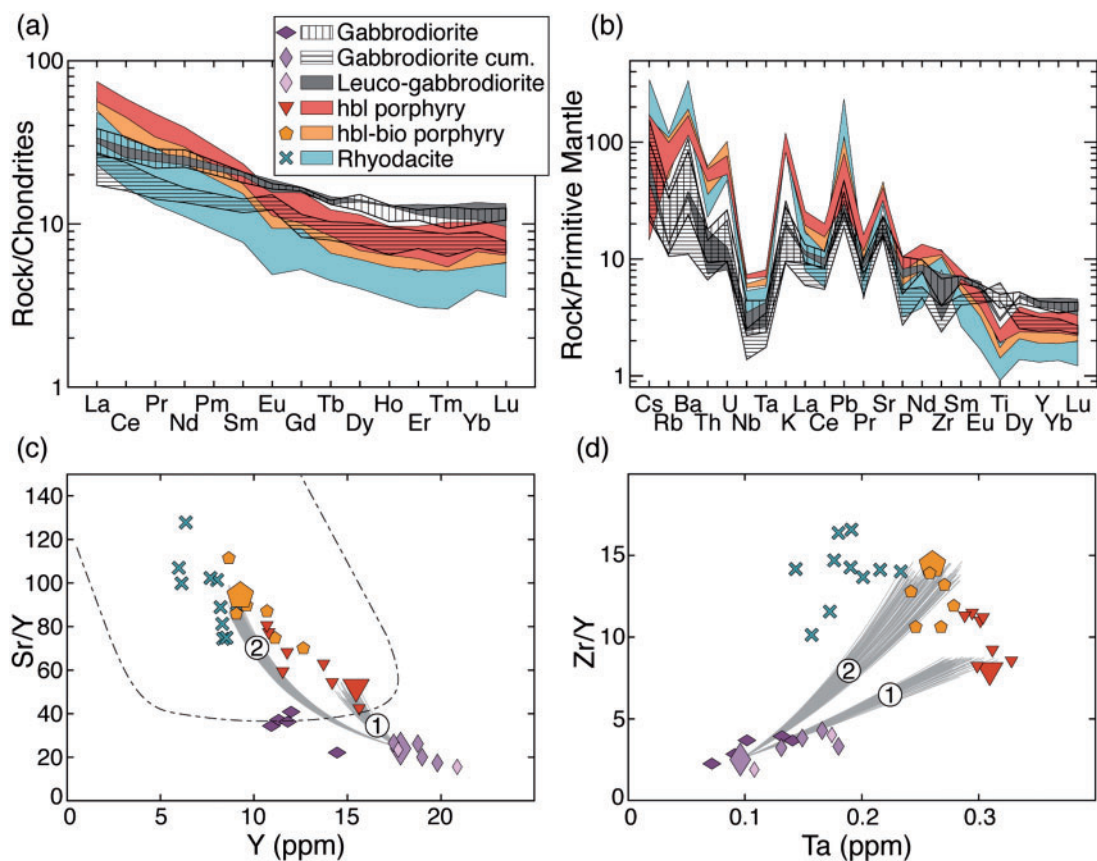
**Fig. 10.** Whole-rock trace element variations. (a) Chondrite-normalized REE patterns [normalizing values from McDonough & Sun (1995)]. (b) Primitive mantle-normalized trace element patterns [normalizing values from McDonough & Sun (1995)]. (c) Y vs Sr/Y. (d) Ta vs Zr/Y. Grey lines in (c) and (d) indicate the AFC paths modeled using a Monte Carlo approach that simultaneously reproduce the trace element composition (REE, Y, Sr, Zr and Ta) of sample 10CC22 (path 1) and sample 10CC94 (path 2). Large symbols highlight end-member compositions used for modeling (see text for details).

## Deep crustal evolution

### The gabbrodiorite complex (GDC)

Owing to the mafic composition of the GDC ($SiO_2 < 52$ wt %), this unit is the one that most closely reflects the signature of its source (i.e. least crustal contamination). In the GDC, the initial zircon Hf isotopic composition ($\varepsilon Hf_i$ of $+10.6$ to $+5.2$; Chelle-Michou et al., 2014) and the whole-rock Nd isotope composition ($\varepsilon Nd_{36\,Ma}$ of $+2.6$ to $+0.9$; Fig. 11a) are not compatible with a 36 Ma depleted mantle source [$\varepsilon Nd$ of $+6$ to $+11$; $\varepsilon Hf$ of $+25$ to $+11$; calculated using present-day values from Workman & Hart (2005)]. However, their Nd and Sr isotopic composition is similar to the most primitive composition of deep crustal xenoliths exhumed near Cusco (including diorite, gabbro and clinopyroxenite; inset Fig. 11a; Chapman et al., 2015). This suggests tha the parental magmas of the GDC were sourced from either sub-arc mantle intensely metasomatized by slab-derived fluids or that the mantle-derived melts intensively interacted with less radiogenic material, probably in a deep crustal hot zone (DCHZ; Annen et al., 2006).

However, the very low Ni ($\sim$10 ppm) and Cr ($\sim$15 ppm) contents and Mg-numbers (42–48) of the GDC indicate that it does not represent the products of

crystallization of primitive mantle melts and that some fractionation of olivine, pyroxene and possibly amphibole has occurred, most probably in the DCHZ. Experimental studies on hydrous ($>$3 wt % $H_2O$) primitive arc basalts at pressure conditions appropriate for the deep crust (0.7–1.2 GPa) show plagioclase to be minimally stable, and that fractionation of olivine, pyroxene and amphibole, as well as possible hybridization with amphibole-bearing lithologies (from previous magma batches) result in the formation of low-Mg, high-Al basalt (MgO $<$ 8 wt % and $Al_2O_3 > 18$ wt %) similar to the gabbrodiorite at Coroccohuayco (Müntener et al., 2001; Nandedkar et al., 2014).

Several lines of evidence indicate that the GDC does not represent a single homogeneous magma batch. These include: (1) evidence of micro-scale mingling between clinopyroxene-rich and orthopyroxene-rich magmas that suggests contrasted initial melt compositions (Fig. 3e and f); (2) variable Sr and Nd isotopic compositions of whole-rock samples (Fig. 11a); (3) heterogeneous Hf isotopic compositions of zircons at the hand sample scale (up to 5 epsilon units; Chelle-Michou et al., 2014); (4) multiple groups of amphiboles at the hand sample scale defined by contrasting concentrations of trace elements (e.g. Zr; Fig. 6c). This suggests
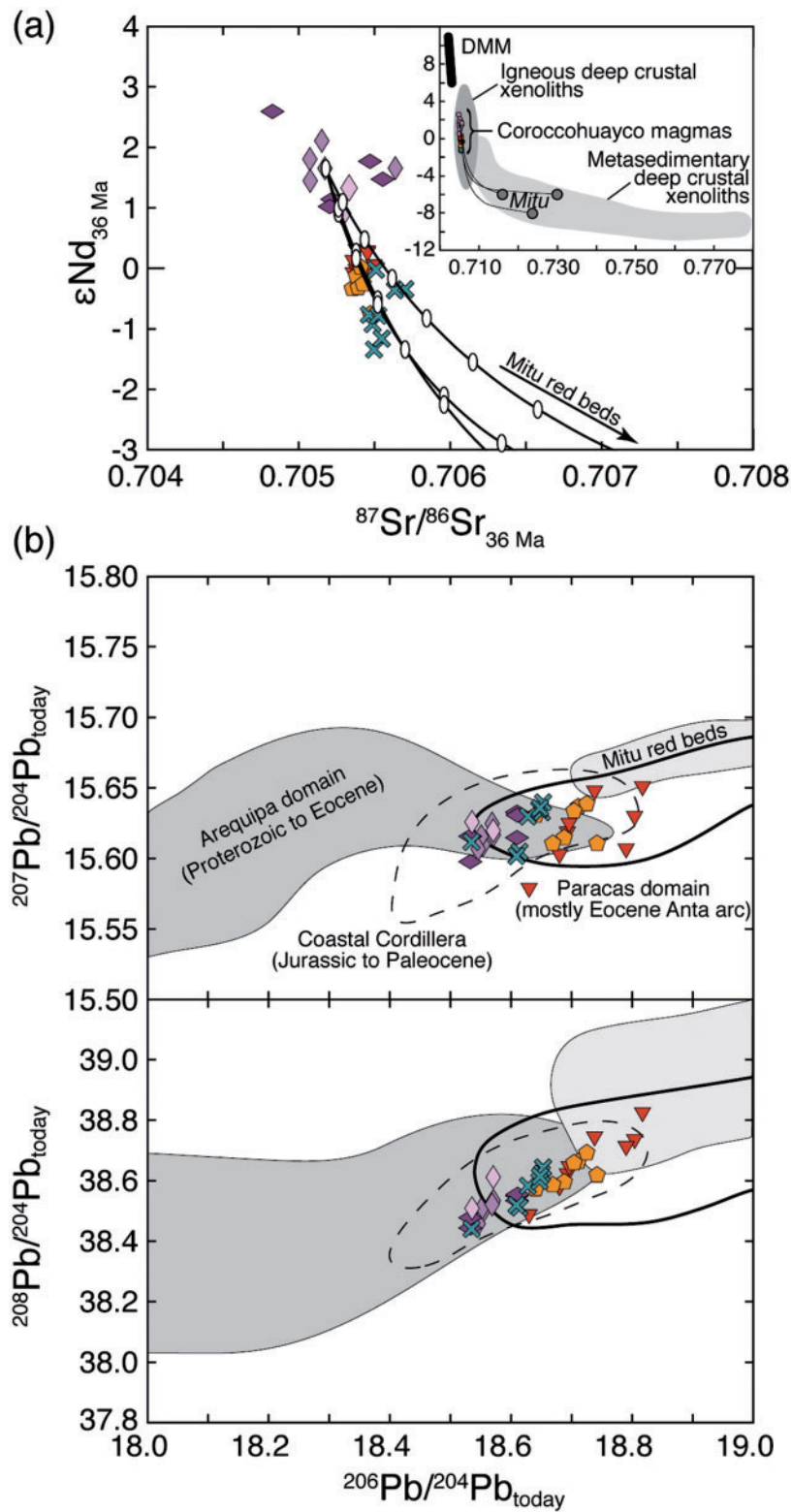
**Fig. 11.** Radiogenic isotope compositions of the studied samples. (a) $^{87}Sr/^{86}Sr$ vs $\varepsilon Nd$ calculated at 36 Ma. Continuous lines represent a simple mixing model with three Triassic red sandstones (from the Mamuera section close to Sicuani) with 10% increments (see text for details). Inset shows the isotopic composition of the Coroccohuayco magmatic rocks compared with depleted MORB source mantle (DMM; data from Workman & Hart, 2005), and metasedimentary and igneous deep crustal xenoliths from the Cusco area (Chapman *et al.*, 2015) all calculated at 36 Ma. (b) Pb isotope plots for samples from Coroccohuayco compared with isotopic reference fields delineated with regional data from Mamani *et al.* (2010). Legend is the same as in Fig. 9.

that the GDC was sourced from one compositionally heterogeneous magma reservoir or from several distinct magma reservoirs within a deep crustal hot zone. Because the GDC marks the beginning of arc magmatism in this region, it would be expected that the DCHZ below the Tintaya district at this time had a lower thermal maturity compared with regions where arc magmatism had persisted at more or less the same position for several millions of years. Under these conditions, it is likely that a newly formed DCHZ hosts several disconnected magma reservoirs, each having a slightly different isotopic composition.

### The porphyries

Compared with other magmatic rocks of the Eocene Anta arc, the dacitic porphyries at Coroccohuayco have higher $Al_2O_3$ ($\sim$17 wt %) and Sr (600–1000 ppm) and lower $Fe_2O_3$, MgO, MnO and $TiO_2$ contents (Fig. 9). This suggests that the porphyries result from magmatic differentiation at mid- to lower crustal levels during which ferromagnesian minerals fractionate from an evolving basalt precursor or are residual during melting of a lower crust amphibolite outside the plagioclase stability field. The generally high Sr/Y values (increasing through time from $\sim$50 for the hornblende porphyry to $\sim$100 for the rhyodacite; Fig. 10c), the moderate La/Yb ($\sim$12) and the listric shape of the chondrite-normalized REE patterns (Fig. 10a) point towards the predominance of amphibole $\pm$ titanite ($\pm$garnet $\pm$ clinopyroxene) in the fractionating mineral assemblage or in the restite. The decreasing Ta and $P_2O_5$ contents with increasing $SiO_2$ (Fig. 9i and k) indicate the predominance of titanite and apatite fractionation, respectively. The small negative Eu anomalies of the porphyries (Fig. 10a) additionally suggest that some plagioclase fractionation may have occurred.

Experimental studies of fractional crystallization of hydrous andesitic and low-Si dacitic melts at 800–450 MPa, 950–850°C and $fO_2$ around the quartz–fayalite–magnetite (QFM) buffer yield dacite and high-Si dacite melts, respectively, through crystallization of amphibole with a lesser amount of plagioclase, garnet (only above 800 MPa), Fe–Ti oxides and pyroxenes (Sisson *et al.*, 2005; Müntener & Ulmer, 2006; McCanta *et al.*, 2007; Alonso-Perez *et al.*, 2009; Nandedkar *et al.*, 2014). Pressures above 800 MPa stabilize garnet at the expense of amphibole (Alonso-Perez *et al.*, 2009), which would result in a higher La/Yb ratio (typically > 20) of the extracted melt. Assuming that these experimental studies apply to the Coroccohuayco magmatic system, they would suggest that the DCHZ was located at pressures around (with a small amount of fractionating garnet) or below (no fractionating garnet) 800 MPa (i.e. at a maximal depth of $\sim$30 km). The crustal thickness of southern Peru in the Eocene is estimated to be 35–40 km, prior to a major orogenic shortening and crustal thickening event in the Miocene (Hindle *et al.*, 2005; Gotberg *et al.*, 2010; Eichelberger *et al.*, 2015), which

would imply that the DCHZ was located within the lower crust.

With respect to the gabbrodiorite complex, the more homogeneous whole-rock Sr and zircon Hf isotopic compositions of the porphyries (Fig. 11a; Chelle-Michou *et al.*, 2014) suggest that they were sourced from a more homogeneous magma reservoir in the DCHZ. Prolonged intracrustal magmatic activity ($\sim$5 Myr) prior to the emplacement of the porphyries (Chelle-Michou *et al.*, 2014) may have favoured thermal maturation of the DCHZ in which large volumes of evolved magma could be generated and homogenized on thousands to millions of years timescales (Sisson *et al.*, 2005; Solano *et al.*, 2012; Melekhova *et al.*, 2013).

## Magma ascent and upper crustal evolution
### The gabbrodiorite complex (GDC)

Petrographic observations (Fig. 3) indicate that the earliest crystallizing phases in the GDC were An90 plagioclase, clinopyroxene and orthopyroxene. Natural observations and experimental studies suggest that such anorthite-rich plagioclase must crystallize near the liquidus at high temperature (1050–1200°C), under hydrous conditions (2–6 wt % $H_2O$) from arc basalts with high Al and/or high $CaO/Na_2O$ values (>8), at various pressures (from 200 to 800 MPa; Sisson & Grove, 1993*a*, 1993*b*; Panjasawatwong *et al.*, 1995; Takagi *et al.*, 2005; Pichavant & Macdonald, 2007; Alonso-Perez *et al.*, 2009; Zellmer *et al.*, 2012; Nandedkar *et al.*, 2014). The low La contents of the An90 plagioclase (La < 1 ppm; Fig. 4c and f) are also in agreement with their crystallization from basaltic melts that have undergone limited fractionation. The negative Eu anomalies of clinopyroxene and orthopyroxene cores (Fig. 7) indicate that they crystallized just after plagioclase, in agreement with hydrous basalt phase diagrams at 200 MPa (e.g. Sisson & Grove, 1993*a*, 1993*b*; Blatter *et al.*, 2013). Their low Al, Ni and Cr contents also confirm that they crystallized at low pressure from a derivative basalt. Clinopyroxene crystallization probably caused a rapid decrease in $CaO/Na_2O$ that triggered a rapid decrease of the plagioclase molar anorthite content to $\sim$An75. Subsequent cooling and crystallization of clinopyroxene and later hornblende explains the normal zoning of plagioclase (Fig. 4b–g).

Towards the south, where the GDC is thicker, an early crystallizing assemblage from now eroded higher levels of the magma chamber probably fractionated from the melt and formed an immature 'cumulate' (the gabbrodiorite cumulate) with anorthite-rich plagioclase and positive Eu anomalies. The lower Zr, $P_2O_5$ and REE + Y concentrations of the gabbrodiorite 'cumulate' compared with the gabbrodiorite, but with similar ratios (e.g. La/Yb, Zr/Y; Figs 9i, j, l and 10; Table 2), cannot be explained by simple crystal accumulation. The higher modal content of poikilitic hornblende (although with slightly lower incompatible element concentrations) relative to plagioclase in the 'cumulate' (Table 1) cannot

explain the lower concentrations in these whole-rock samples. The low Zr and $P_2O_5$ concentrations in the 'cumulate' suggest that these samples host on average 30–50% less zircon and apatite than the gabbrodiorite. Thus, because zircon and apatite are large repositories of REE + Y (Bea, 1996), the lower whole-rock REE + Y contents of the gabbrodiorite 'cumulate' are most probably due to lower amounts of zircon and apatite. This implies that the interstitial melt from which these minerals crystallized (as well as possibly some hornblende) was compositionally zoned at the scale of the GDC. In this scenario, the more evolved melt (incompatible element-rich) formed the gabbrodiorite, whereas the less evolved melt (incompatible-poor) formed the gabbrodiorite 'cumulate'.

An90 plagioclase–liquid hygrometry (Lange *et al.*, 2009) at a near-liquidus temperature of 1200°C yields a melt water content of around 3 wt % (for a melt composition similar to the whole-rock gabbrodiorite samples). In turn, hornblende hygrometry (Ridolfi & Renzulli, 2012) yields melt water contents of around 5 wt %, which is the water solubility of an andesitic melt at around 200 MPa (e.g. Newman & Lowenstern, 2002; Papale *et al.*, 2006). These contrasted hygrometry results, together with the early and late crystallization of An90 plagioclase and hornblende, respectively, suggest that volatile saturation was promoted by isobaric plagioclase crystallization from a melt containing initially $\sim$3 wt % dissolved $H_2O$. Mass-balance considerations require that about 40 wt % of anhydrous minerals (plagioclase, Fe–Ti oxides, pyroxenes) crystallize prior to amphibole saturation. This is consistent with both textural observations (Fig. 3) and the modal mineralogy (Table 1) of the gabbrodiorite.

The volumetrically minor leuco-gabbrodiorite is more evolved than the gabbrodiorite and has similar trace (including REE and Eu/Eu*) and minor element chemistry (Figs 9 and 10; Table 2). Plagioclases in the leuco-gabbrodiorite are much more albitic than those from the gabbrodiorite and are in equilibrium with hornblendes in the same samples (Fig. 5b). This suggests that the leuco-gabbrodiorite magma does not result from advanced fractionation of the gabbrodiorite magma in the upper crust, which would be dominated by plagioclase and amphibole and would significantly change the trace element signature of the melt. Instead, we propose that it acquired its composition through fractional crystallization of ferromagnesian minerals, mostly Fe–Ti oxides and pyroxenes, probably in the deep crust.

### The porphyries

It is important to stress that, in line with established models for porphyry deposits (Dilles & Proffett, 1995; Shinohara & Hedenquist, 1997; Sillitoe, 2010), the porphyries from which we obtained samples probably represent small apophyses of a larger pluton lying at greater depth and that the majority of the rock-forming

minerals originated from this pluton. The emplacement pressure of this magmatic (granitic, *sensu lato*) body as constrained by hornblende barometry is around 250–100 MPa (Fig. 12d–f), which is typical for plutons underlying porphyry systems (e.g. Dilles, 1987; Cloos, 2001; Stavast *et al.*, 2008; Sillitoe, 2010; Steinberger *et al.*, 2013). At such pressures a silicic melt is water saturated at $5 \pm 1$ wt % (Fig. 12d and e; Papale *et al.*, 2006). Although Erdmann *et al.* (2014) showed that the calibration of Ridolfi & Renzulli (2012) does not reliably predict the melt $H_2O$ content at the Mount Merapi volcano, water content calculated by hornblende hygrometry in the porphyries at Coroccohuayco (Fig. 12e) is perfectly consistent with water saturation of the melt at 250–100 MPa.

A previous study of the Hf isotopic compositions and ages of zircon xenocrysts and antecrysts from the porphyries at Coroccohuayco (Chelle-Michou *et al.*, 2014) has highlighted that the upper crustal magmatic evolution of the felsic magmas is characterized by open-system behaviour and dominated by crustal assimilation, proto-pluton cannibalism and magma recharge. U–Pb age spectra of zircon xenocrysts and xenocrystic cores from the porphyries show that during upper crustal evolution, the magmas assimilated Triassic siliciclastic sediments (Mitu group; Chelle-Michou *et al.*, 2014). Furthermore, zircons (autocrysts and antecrysts) from the porphyries display a temporal decrease in initial $\varepsilon$Hf from $\sim$7 at 37·5 Ma to $\sim$4 at 35·6 Ma, consistent with progressive assimilation of these sediments (with zircon $\varepsilon Hf_{36\ Ma}$ of 0 to –6). Such Triassic sediments (red sandstones, conglomerates and pelites) crop out 60 km NE of Coroccohuayco at the border of the Mesozoic and Cenozoic basins within which the Andahuaylas–Yauri Batholith was emplaced. Crustal assimilation is also highlighted by initial isotopic compositions of Sr and Nd that become increasingly crustal-like with time (Fig. 11a). A simple mixing model between a magma with the isotopic composition of gabbrodiorite sample 10CC55 and the Sr and Nd concentrations of the porphyries and the Mitu sediments suggests that the isotopic composition of the porphyries is best explained by 20–30% bulk assimilation of the sediments (Fig. 11a). Thermodynamic models of assimilation–fractional crystallization (AFC) indicate that this is an unrealistic amount of assimilation under the estimated *P–T* conditions of the upper crust (e.g. Glazner, 2007). One possibility to explain this inconsistency would be that the upper crustal magmatic system underwent periodic recharge that allowed the maintenance of high temperatures and promoted crustal assimilation (e.g. Spera & Bohrson, 2004). Some amount of reactive bulk assimilation in which the assimilant partly remains in solid form may also provide a mechanism for lower energy assimilation (e.g. Beard *et al.*, 2005; Erdmann *et al.*, 2010). Alternatively, the isotopic composition of the parental magma at 36 Ma (before assimilation) may have been more evolved than that of the gabbrodiorite, possibly owing to the involvement of a
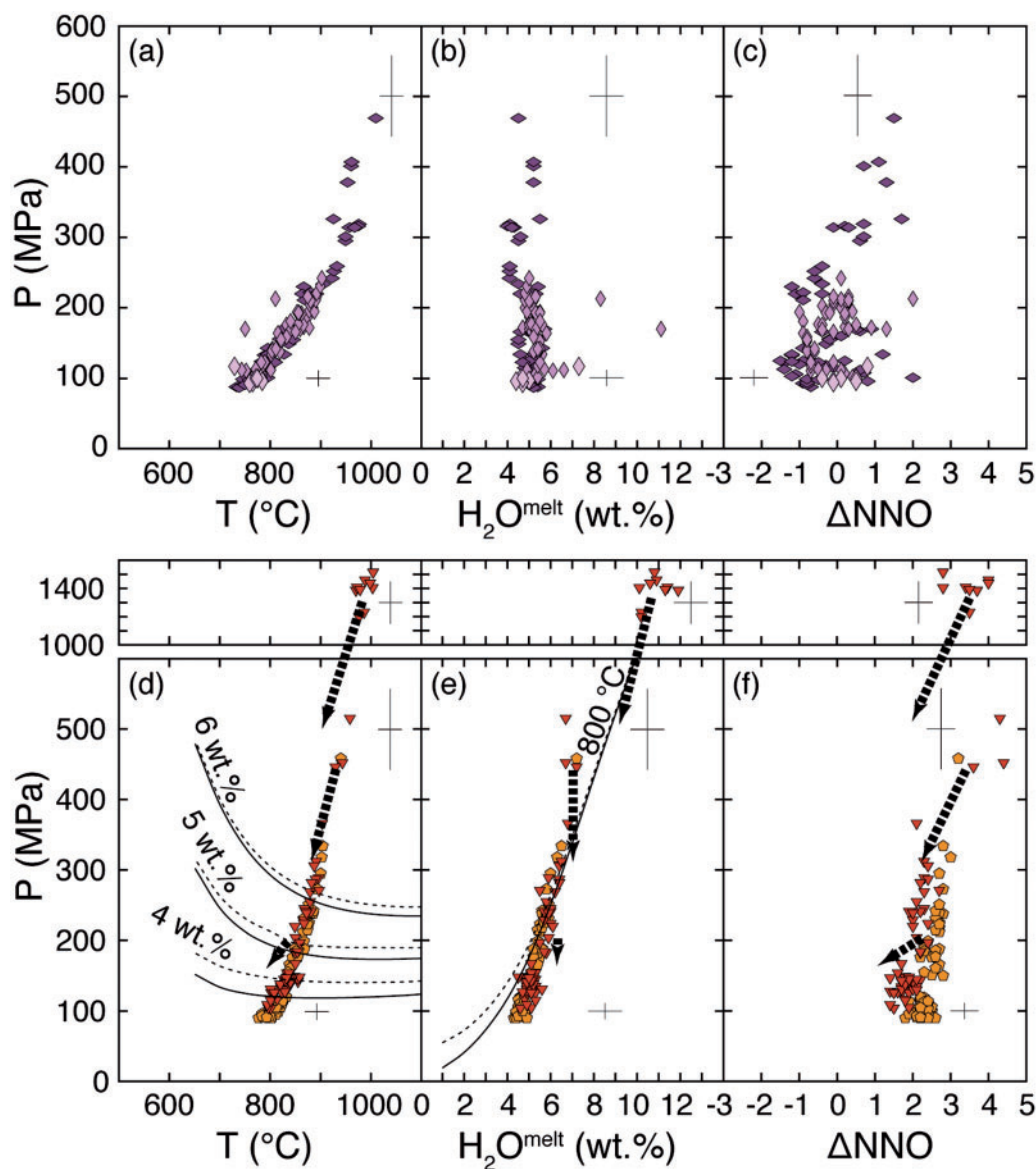
**Fig. 12.** Plot of *P* vs (a, d) *T*, (b, e) H$_2$O$_{melt}$, and (c, f) *f*O$_2$ (expressed as ΔNNO) calculated from the amphibole-only formulations of Ridolfi & Renzulli (2012) for amphiboles that match the compositional calibration range. Error bars are model uncertainties. Curves represent H$_2$O solubility calculated for 10 ppm CO$_2$ (continuous line) and 100 ppm CO$_2$ (dashed line) using the model of Papale *et al.* (2006) with the average composition of the hornblende porphyry. Dashed arrows indicate the effect of the maximal Na-correction on the calculated parameters for the high-Al, intermediate-Al and low-Al amphiboles in the porphyritic rocks (see text and Fig. 13). Legend is the same as in Fig. 5.

greater amount of deep crustal material than in the GDC and/or of a higher amount of slab-derived material in the fluids metasomatizing the sub-arc mantle. Another possibility could be that the Mitu samples that we analysed are not representative of the composition of the rocks assimilated at Coroccohuayco. We should also keep open the possibility that the assimilated Mitu sediments were not located in the upper crust but in the deep crust, as recently suspected near Cusco on the basis of felsic granulite xenoliths sampled by Pliocene to Quaternary volcanism (Chapman *et al.*, 2015). Under this hypothesis, such an amount of crustal assimilation in a DCHZ can readily happen after a few hundred thousand to millions

of years of magma injection (Thompson *et al.*, 2002; Annen *et al.*, 2006).

Porphyry samples have a concordant zircon age record spanning nearly 2 Myr, from 37·5 to 35·6 Ma; this has been interpreted to reflect cannibalism of previously emplaced magma batches (or proto-plutons; Chelle-Michou *et al.*, 2014). The high-Al amphiboles found in the hornblende porphyry are also interpreted in terms of proto-pluton cannibalism. Indeed, these amphiboles record Na-corrected pressures of 800 to 500 MPa and melt water content around 8 wt % (Figs 12e and 13a, c), which is close to the solubility of water in a dacitic melt at this pressure. The high melt
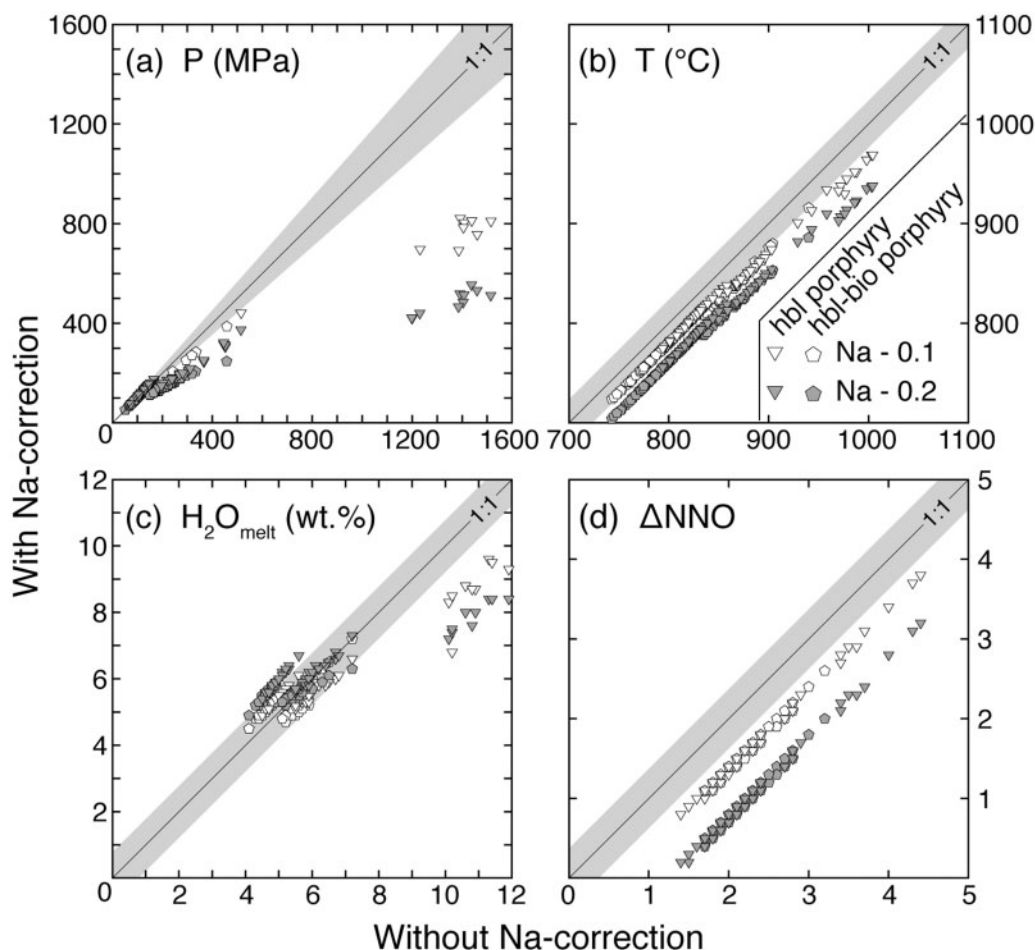
**Fig. 13**. Effect of correcting for amphibole excess $Na_A$ on the results of (a) pressure, (b) temperature, (c) melt water content and (d) oxygen fugacity calculations for the hornblende and hornblende–biotite porphyries. Open symbols correspond to calculations performed with an Na decrease of 0·1 p.f.u. Filled symbols correspond to calculations performed with an Na decrease of 0·2 p.f.u. Shaded areas refer to model uncertainties, which are $P \pm 11.5\%$, $T \pm 23.5°C$, $H_2O_{melt} \pm 0.78$ wt % and NNO $\pm 0.37$ log units (Ridolfi & Renzulli, 2012).

water content is consistent with the high Ba/La and Sr content of these amphiboles. This suggests that the magma from which these amphiboles crystallized reached volatile saturation in the deep to middle crust, which induced rapid and abundant crystallization and inhibited magma ascent to shallower levels. These amphiboles were probably sampled by subsequent magma batches at 35·6 Ma and transferred to upper crustal levels.

Textures of titanite and K-feldspar also highlight open-system evolution in the porphyries. Although some titanite may have fractionated in the deep crust, some hornblendes crystallized in the upper crust retain a record of titanite co-crystallization. Indeed, some hornblendes from the hornblende porphyry with high-MREE–HREE–Y–Ta cores (circled points in Fig. 6g, i and j; with Na-corrected pressure around 150 MPa) evolving to lower MREE–HREE–Y–Ta rims (part of the main amphibole group in Fig. 6g, i and j) show that at least part of the titanite crystallization took place in the early stage of upper crustal evolution upon intrusion of the dacitic magma. This is consistent with the presence

of titanite inclusions in hornblendes and biotites. Titanites that display dissolution–recrystallization textures (Fig. 8h) indicate that their early cores were destabilized, probably upon hot magma recharge. Titanite hosting ilmenite–hematite droplets along growth surfaces (Fig. 8h) may indicate fluctuating oxygen fugacity (e.g. McLeod *et al.*, 2011), possibly as a result of episodic fluid exsolution (Burgisser & Scaillet, 2007) or recharge by more reduced magma. Petrographic observations show that K-feldspar was a late crystallizing phenocryst in the porphyries (Fig. 8i and j). The Ba zoning of K-feldspar phenocrysts from the hornblende–biotite porphyry and the rhyodacite, which displays a smooth decrease and an abrupt increase at dissolution–recrystallization surfaces (Fig. 8i), also suggests the occurrence of magma recharge during K-feldspar crystallization.

Finally, the zircon record of the rhyodacite porphyry proves that remelting of proto-plutons was an important process at Coroccohuayco. Indeed, most zircons from the rhyodacite crystallized *c.* 0·5 Myr before the supposed emplacement of this porphyry as constrained

by cross-cutting relationship with the hornblende and hornblende–biotite porphyries (Chelle-Michou *et al.*, 2014). The Nd and Sr isotopic compositions of this rock also show that it records the maximal amount of crustal assimilation (Fig. 11a). We propose that magma recharge may have triggered partial melting of previous magma batches (proto-plutons) and crustal material (Mitu sediments), possibly hybridized with these partial melts, finally yielding modified magma compositions.

Overall, the magnitude of crustal assimilation, proto-pluton cannibalism and remelting appears to have increased with time in the felsic magmatic system at Coroccohuayco, from the inception of intracrustal magmatism at ~37·5 Ma to the emplacement of the porphyries at ~35·6 Ma. This requires an increasing amount of heat to be added to the system. We propose that sustained and possibly increasing magmatic injections in the upper crust for 2 Myr before the emplacement of the porphyries (as evidenced by zircon antecrysts) could have favoured the thermal maturation of the system and increased the local geothermal gradient that peaked at the time of porphyry emplacement. Under these conditions, convective melting of roof-blocks (proto-plutons and/or older crust) and/or remobilization and mingling or mixing of crystal mush by hot magma during high flux recharge events may be facilitated. This could provide a mechanism for efficient crustal assimilation and proto-pluton cannibalism and re-melting (Reubi & Blundy, 2008; Schmitt *et al.*, 2010; Chiaradia *et al.*, 2011, 2014; Reubi *et al.*, 2011; Kennedy *et al.*, 2012; Simakin & Bindeman, 2012; Cashman & Blundy, 2013; Walker *et al.*, 2013). In addition, a large part of the crustal assimilation might have occurred in the DCHZ through 2 Myr of mantle-derived magma injection.

The nature of the recharge magma in the upper crust is unclear. Crustal assimilation and proto-pluton cannibalism would readily be facilitated by mafic magma recharges. However, we could not find any compelling evidence for the involvement of such mafic magma at Coroccohuayco. Alternatively, we could envision intermediate to felsic recharge magma that would in any case be hotter than the cooling magmatic system into which it intrudes. The efficiency of cannibalism and assimilation would then critically depend on flux and volume of the recharge events. Combining zircon age data and thermal modelling, Caricchi *et al.* (2014) estimated that the volume of such a felsic magma body associated with the porphyries could be of the order of 500–2000 km³, consistent with such potential high-volume recharge events.

## Quantitative constraints on the evolutionary path of the Coroccohuayco magmatic suite from trace element modelling

To strengthen the petrological model depicted above we have modelled the end-member whole-rock trace element compositions (REE, Y, Sr, Ta, Zr) in terms of AFC processes (DePaolo, 1981). Starting with the most

primitive gabbrodiorite composition (10CC55), we modelled the evolution to the hornblende (10CC22) and hornblende–biotite (10CC94) porphyries as an average of upper and deep crustal processes. To overcome the large uncertainties associated with numerous input parameters we used a Monte Carlo approach; this consists of generating a large number of outputs by randomly selecting the input parameters within known possible ranges. To obtain internally consistent sets of partition coefficients for the $REE^{3+} + Y^{3+}$ we generated them using lattice strain fitting (Blundy & Wood, 2003) from available sets of partition coefficients. The Sr, Zr and Ta partition coefficients were selected within a range of published values [see Béguelin *et al.* (2015) for more details on the method]. The fractionating assemblages were chosen according to the mineralogy and petrography of the samples. However, for the porphyries, because part of the fractionation probably happened in the deep crust and at least part of the corresponding fractionating assemblage may not be accessible (e.g. garnet, clinopyroxene?), the fractionating assemblage must be inferred from experimental data (e.g. Müntener & Ulmer, 2006). For the porphyries, the assimilant was modelled with various proportions of Mitu sediments and proto-pluton partial melts that were assumed to be similar to the rhyodacite. Simulations that reproduced simultaneously all the trace elements of the targeted samples within 10–20% (depending on the element) were considered valid. Results are presented in Fig. 10c and d, Table 3, and SD Tables 6 and 7.

The modelling results show that the chemistry of the porphyries is consistent with fractionation dominated by amphibole and pyroxene with lesser amounts of plagioclase. Fractionation of apatite and titanite is poorly constrained by the model and is better suggested by the whole-rock data (i.e. decreasing $P_2O_5$ and Ta with increasing $SiO_2$; Fig. 9i and k). Interestingly, the successful models require the presence of 1·2–5·8 wt % of garnet in the bulk fractionating assemblage (Table 3). This amount of fractionating garnet indicates that deep crustal fractionation processes occurred at around 800 MPa (*c.* 30 km depth), where the assemblage amphibole + pyroxene + plagioclase ± garnet is stable (e.g. Alonso-Perez *et al.*, 2009). As expected, trace element modelling did not help in constraining the amount of assimilation (e.g. Powell, 1984) and the relative proportion of assimilants. The evolution from the hornblende porphyry to the hornblende–biotite porphyry was caused by more extensive hornblende fractionation, mostly at the expense of plagioclase. This most probably reflects limited evolution at upper crustal levels and more extensive deep crustal evolution for the hornblende–biotite porphyry with respect to the hornblende porphyry.

## Evidence for coeval uplift and erosion

Amphibole crystallization pressure for the GDC (250–100 MPa) and the porphyries (250–100 MPa) are

**Table 3:** Summary of results from the AFC Monte Carlo simulations

| | $F$ ($M_m/M_0$) | $r$ ($M_a/M_c$) | Assimilant | Amph (%) | Garnet (%) | Plag (%) | Apatite (%) | Titanite (%) | Cpx (%) | Opx (%) |
|---|---|---|---|---|---|---|---|---|---|---|
| *Input* | | | | | | | | | | |
| Minimum | 0·1 | 0 | 1 | 0 | 0 | 0 | 0 | 0 | 0 | 0 |
| Maximum | 0·6 | 1 | 1 | 80 | 5 | 50 | 1 | 1 | 30 | 5 |
| *10CC55 to 10CC22* | | | | | | | | | | |
| Minimum | 0·34 | 0·05 | 0·13 | 34·7 | 1·2 | 5·0 | 0·00 | 0·01 | 25·5 | 0·2 |
| Average | 0·36 | 0·10 | 0·57 | 45·4 | 2·5 | 11·5 | 0·15 | 0·26 | 37·0 | 3·2 |
| Maximum | 0·40 | 0·15 | 0·99 | 57·9 | 5·0 | 21·0 | 0·58 | 0·99 | 49·4 | 6·3 |
| *10CC55 to 10CC94* | | | | | | | | | | |
| Minimum | 0·30 | 0·02 | 0·01 | 54·1 | 1·4 | 0·0 | 0·00 | 0·00 | 16·4 | 0·0 |
| Average | 0·33 | 0·05 | 0·47 | 63·3 | 2·8 | 2·7 | 0·49 | 0·25 | 27·3 | 3·2 |
| Maximum | 0·34 | 0·08 | 0·99 | 77·4 | 5·8 | 5·8 | 0·95 | 0·62 | 36·7 | 6·2 |

Assimilant: $0 = 100\%$ of average rhyodacite; $1 = 100\%$ of average Mitu sediments. $F$ is final mass of the melt ($M_m$) over the initial mass ($M_0$). $r$ is assimilated mass ($M_a$) over the crystallized mass ($M_c$).

equivalent (Fig. 12). However, whereas the amphiboles from the GDC crystallized *in situ* at *c.* 40·2 Ma, amphiboles from the porphyries were sampled at *c.* 35·6 Ma from a pluton lying at some depth below the GDC and transferred into small stocks and dykes. The porphyritic intrusions and the associated copper mineralization are now juxtaposed to the GDC. These observations suggest that erosion was taking place in the Tintaya district between 40·2 and 35·6 Ma.

Based on fluid inclusion data and textural observation of the skarn and breccia, Maher (2010) proposed that the ore deposit formed at pressures around 25 MPa. This indicates that 75 (100–25) to 225 (250–25) MPa of unloading occurred between 40·2 and 35·6 Ma. This corresponds to an exhumation rate of 0·6–1·8 mm $a^{-1}$. Such erosion rates are higher than those measured today in the Andes (e.g. Gregory-Wodzicki, 2000; Safran *et al.*, 2005; Bookhagen & Strecker, 2012) but are in the range of those observed in other porphyry systems (e.g. Houston & Dilles, 2013). They are also consistent with the rapid subsidence and infill of the coeval Eocene sedimentary basins in the future Altiplano region associated with the Incaic compressional event (Carlotto, 2013; Chelle-Michou *et al.*, 2015; Horton *et al.*, 2015). These observations confirm that the Coroccohuayco deposit formed during a period of intense exhumation and erosion similar to porphyry systems worldwide (e.g. Skewes & Stern, 1994; Tosdal & Richards, 2001; Richards, 2003; Cooke *et al.*, 2005; Chiaradia *et al.*, 2009b; Sillitoe, 2010; Schütte *et al.*, 2011).

## THE ROLE OF MAGMATIC PROCESSES IN THE GENESIS OF THE COROCCOHUAYCO ORE DEPOSIT

Similar to porphyry-related magmatism elsewhere (e.g. Richards & Kerrich, 2007; Loucks, 2014), the magmatic rocks temporally associated with the mineralization (the porphyries) display a high Sr/Y signal as opposed to the precursor magmas (Fig. 10c). This is interpreted to reflect hydrous magma evolution in the mid- to deep crust where amphibole $\pm$ garnet are more stable than

plagioclase (Rohrlach & Loucks, 2005; Richards, 2011a; Chiaradia *et al.*, 2012; this study). The common association of high Sr/Y magma and porphyry Cu deposits suggests that the fertility of the magmatic system was mostly acquired in the DCHZ (e.g. Richards, 2011a; Chiaradia *et al.*, 2012; Chiaradia, 2014). Magmatic evolution in the DCHZ was probably responsible for increasing magma water content from 3 wt % in the basaltic magma to 5 wt % in the felsic magma (Fig. 14).

Concurrent with the increase in the water content, the magma oxidation state increased from NNO to around NNO + 1 to NNO + 2 (Fig. 14). During such a transition in $fO_2$ the dominant sulphur species rapidly changes from $S^{2-}$ to $S^{6+}$ (Jugo *et al.*, 2010), the latter being one order of magnitude more soluble in silicate melts (Jugo, 2009), allowing chalcophile elements (such as Cu) to behave incompatibly during magmatic evolution. This is probably a key factor for the genesis of a porphyry Cu deposit (e.g. Ishihara, 1981; Candela, 1992; Lynton *et al.*, 1993; Richards, 2003) such as Coroccohuayco. The reasons for this higher oxygen fugacity remain unclear. On a global scale water and element tracers of slab-derived fluids have been found to correlate with $fO_2$ in primitive melts of the mantle wedge (Kelley & Cottrell, 2009). However, the high water and LILE contents (e.g. Ba) observed in the porphyries (Figs 10b and 12e) can be attained by recharge–assimilation–fractional crystallization processes and do not require additional input of oxidized slab-derived fluid (e.g. Chiaradia *et al.*, 2014). Some researchers have proposed that the sub-arc mantle may become increasingly oxidized after several millions years of slab fluid metasomatism (Rowe *et al.*, 2009; Evans & Tomkins, 2011; Evans *et al.*, 2012). On the other hand, trace element systematics suggests that the sub-arc mantle may not be more oxidized than mid-ocean ridge basalt (MORB)-source mantle (Lee *et al.*, 2005, 2010, 2012; Mallmann & O'Neill, 2009). These contradictory views highlight the need for continued efforts to understand the process leading to high oxygen fugacity in arc magmas that favours the genesis of porphyry deposits (e.g. Richards, 2015). The increase in $fO_2$ recorded at Coroccohuayco may be explained by fractional
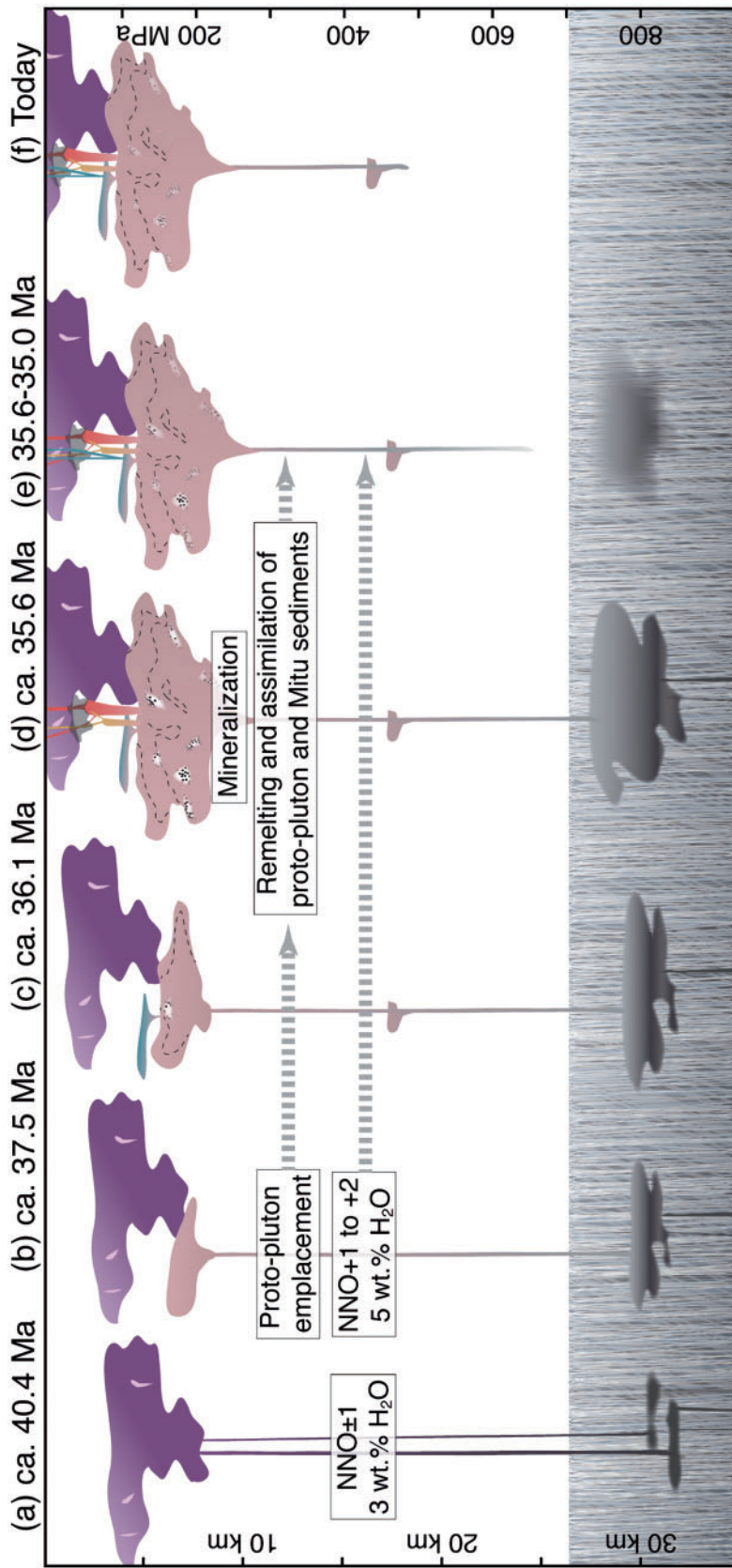
**Fig. 14.** Schematic petrogenetic model for the Coroccohuayco magmatic suite. (a) Emplacement of the GDC from a heterogeneous source in the deep crust. Some amount of differentiation in the upper crust generated the gabbrodiorite and the gabbrodiorite 'cumulate' rocks. The leuco-gabbrodiorite probably represents a more evolved magma from the deep crust. (b) Emplacement of a deep-seated proto-pluton. (c) Growth of proto-pluton by injection of new magma batches sourced from a large and homogeneous deep crustal hot zone. Transitory periods of crustal and proto-pluton assimilation triggered by new magma batches. (d) Sustained recharge of pristine silicic magma from the deep crust (i.e. uncontaminated magma) where it acquired most of its chemical characteristic through mostly amphibole + clinopyroxene + plagioclase ± garnet fractionation (i.e. high Sr/Y). Increasing amount of proto-pluton cannibalism and crustal assimilation dominantly in the upper crust. Porphyry emplacement occurred at peak thermal conditions followed by ore-forming fluid exsolution. Remelting of the early laccolith probably started at this time and may have been caused by heating from the underlying magma reservoir. (e) Remelting of the laccolith continued until it could be remobilized and emplaced as a rhyodacite (f) Situation today with the outcropping Coroccohuayco magmatic suite, near-surface ore body and its deep-seated plutonic root. From (a) to (e) erosion of 2·8–6·6 km occurred in response to uplift associated with the Incaic orogenic event.

crystallization, degassing, assimilation, varying amounts of slab-fluid metasomatism of the mantle source, or a combination of these [see review by Richards (2015)]. However, we note that the hypothesis that the Triassic Mitu red beds or other oxidized sediments could be located in the DCHZ (see Chapman et al., 2015) instead of in the upper crust (Chelle-Michou et al., 2014) means that their efficient assimilation could readily drive the observed increase in $fO_2$.

Sustained upper crustal magmatism from 37·5 to 35·6 Ma appears to have increasingly favoured crustal assimilation and proto-pluton cannibalism. This necessarily implies that a large volume of magma (of the order of 1000 km$^3$; Caricchi et al., 2014) was emplaced in the crust, which constituted a large reservoir of copper and sulphur able to source the Coroccohuayco mineral deposit. The resulting thermal anomaly was greatest just before the mineralization event and probably favoured slow cooling of the underlying silicic magma body and more efficient metal diffusion and partitioning into exsolving fluids (Stavast, 2006; Vigneresse, 2007). If previous magma batches were able to saturate and sequester some amount of sulfides, subsequent cannibalism of these sulfide-bearing domains may contribute to the final metal budget of the deposit (Wilkinson, 2013). A similar process could also occur in the deep crust where several million years of magmatism could build up a sulfide-enriched reservoir (Lee et al., 2012; Chiaradia, 2014). Subsequent remobilization of these sulphides and transfer to the upper crust could also contribute to the magma metal endowment.

## CONCLUSIONS

Figure 14 presents a general model for the evolution of the Coroccohuayco magmatic system based on age constraints from Chelle-Michou et al. (2014). At c. 40·4 Ma the GDC magmas were sourced from a heterogeneous deep crustal hot zone and subsequently underwent minor degrees of differentiation in the upper crust to yield the gabbrodiorite and the gabbrodiorite 'cumulate'. The leuco-gabbrodiorite was probably sourced from the same deep crustal magma chamber that underwent a slightly higher degree of differentiation. After a magmatic lull, magmatism resumed at c. 37·5 Ma with the injection of several magma batches within the upper crust, probably sourced from a more mature and homogeneous deep crustal hot zone. The compositions of these magmas were mostly acquired in the deep crust but some amount of fractionation and assimilation also occurred in the upper crust. Sustained magma injection (recharge) until c. 35·6 Ma favoured upper (and to some extent mid-) crustal assimilation of previous magma batches (proto-plutons) and of older crust. Because the porphyries record increasing amounts of assimilation with time they are thought to have been extruded from an upper crustal silicic magma reservoir undergoing steadily increasing thermal maturation. The rhyodacite results from partial remelting of a proto-pluton, as suggested by zircon high-precision U–Pb geochronology and cross-cutting relationships. Partial melt similar to the rhyodacite is likely to have hybridized with pristine (uncontaminated), deep crustal silicic melt. This magmatic history is coeval with active erosion probably associated with uplift caused by the Incaic compressional event. The fertility of the felsic magma with respect to porphyry genesis was probably acquired in the deep crust through the increase of water content and oxygen fugacity in the melt and associated S and Cu enrichment. Proto-pluton cannibalism and building of a stable thermal anomaly in the upper crust may have favoured Cu and S recycling as well as their efficient extraction from the magma to form the ore deposit.

## SUPPLEMENTARY DATA

Supplementary data for this paper are available at *Journal of Petrology* online.

## REFERENCES

Alonso-Perez, R., Müntener, O. & Ulmer, P. (2009). Igneous garnet and amphibole fractionation in the roots of island arcs: experimental constraints on andesitic liquids. *Contributions to Mineralogy and Petrology* **157**, 541–558.

Anderson, J. L. & Smith, D. R. (1995). The effects of temperature and $fO_2$ on the Al-in-hornblende barometer. *American Mineralogist* **80**, 549–559.

Anderson, J. L., Barth, A. P., Wooden, J. L. & Mazdab, F. (2008). Thermometers and thermobarometers in granitic systems. In: Putirka, K. D. & Tepley, F. J., III (eds) *Minerals, Inclusions and Volcanic Processes. Mineralogical Society of America and Geochemical Society, Reviews in Mineralogy and Geochemistry* **69**, 121–142.

Annen, C., Blundy, J. D. & Sparks, R. (2006). The genesis of intermediate and silicic magmas in deep crustal hot zones. *Journal of Petrology* **47**, 505–539.

Arriagada, C., Roperch, P., Mpodozis, C. & Cobbold, P. R. (2008). Paleogene building of the Bolivian Orocline: Tectonic restoration of the central Andes in 2-D map view. *Tectonics* **27**, TC6014.

Bea, F. (1996). Residence of REE, Y, Th and U in granites and crustal protoliths; implications for the chemistry of crustal melts. *Journal of Petrology* **37**, 521–552.

Beard, J. S., Ragland, P. C. & Crawford, M. L. (2005). Reactive bulk assimilation: A model for crust–mantle mixing in silicic magmas. *Geology* **33**, 681–684.

Béguelin, P., Chiaradia, M., Beate, B. & Spikings, R. (2015). The Yanaurcu volcano (Western Cordillera, Ecuador): A field, petrographic, geochemical, isotopic and geochronological study. *Lithos* **218–219**, 37–53.

Blatter, D. L., Sisson, T. W. & Hankins, W. B. (2013). Crystallization of oxidized, moderately hydrous arc basalt at mid- to lower-crustal pressures: implications for andesite genesis. *Contributions to Mineralogy and Petrology* **166**, 861–886.

Blundy, J. D. & Wood, B. (2003). Partitioning of trace elements between crystals and melts. *Earth and Planetary Science Letters* **210**, 383–397.

Blundy, J., Mavrogenes, J., Tattitch, B., Sparks, S. & Gilmer, A. (2015). Generation of porphyry copper deposits by gas–brine reaction in volcanic arcs. *Nature Geoscience* **8**, 235–240.

Bookhagen, B. & Strecker, M. R. (2012). Spatiotemporal trends in erosion rates across a pronounced rainfall gradient: Examples from the southern Central Andes. *Earth and Planetary Science Letters* **327–328**, 97–110.

Burgisser, A. & Scaillet, B. (2007). Redox evolution of a degassing magma rising to the surface. *Nature* **445**, 194–197.

Candela, P. A. (1992). Controls on ore metal ratios in granite-related ore systems: an experimental and computational approach. *Transactions of the Royal Society of Edinburgh: Earth Sciences* **83**, 317–326.

Caricchi, L., Simpson, G. & Schaltegger, U. (2014). Zircons reveal magma fluxes in the Earth's crust. *Nature* **511**, 457–461.

Carlotto, V. (1998). Evolution andine et raccourcissement au niveau de Cusco (13°–16°S), Pérou: Enregistrement sédimentaire, chronologie, contrôles paléogéographiques, évolution cinématique. PhD thesis, Université Joseph Fourier, Grenoble, 199 pp.

Carlotto, V. (2013). Paleogeographic and tectonic controls on the evolution of Cenozoic basins in the Altiplano and Western Cordillera of southern Peru. *Tectonophysics* **589**, 195–219.

Cashman, K. & Blundy, J. D. (2013). Petrological cannibalism: the chemical and textural consequences of incremental magma body growth. *Contributions to Mineralogy and Petrology* **166**, 703–729.

Chapman, A. D., Ducea, M. N., McQuarrie, N., Coble, M., Petrescu, L. & Hoffman, D. (2015). Constraints on plateau architecture and assembly from deep crustal xenoliths, northern Altiplano (SE Peru). *Geological Society of America Bulletin*, doi: 0.1130/B31206.1.

Chelle-Michou, C., Chiaradia, M., Ovtcharova, M., Ulianov, A. & Wotzlaw, J.-F. (2014). Zircon petrochronology reveals the temporal link between porphyry systems and the magmatic evolution of their hidden plutonic roots (the Eocene Coroccohuayco deposit, Peru). *Lithos* **198–199**, 129–140.

Chelle-Michou, C., Chiaradia, M., Selby, D., Ovtcharova, M. & Spikings, R. A. (2015). High-resolution geochronology of the Coroccohuayco porphyry–skarn deposit, Peru: a rapid product of the Incaic orogeny. *Economic Geology* **110**, 423–443.

Chiaradia, M. (2014). Copper enrichment in arc magmas controlled by overriding plate thickness. *Nature Geoscience* **7**, 43–46.

Chiaradia, M., Merino, D. & Spikings, R. (2009a). Rapid transition to long-lived deep crustal magmatic maturation and the formation of giant porphyry-related mineralization (Yanacocha, Peru). *Earth and Planetary Science Letters* **288**, 505–515.

Chiaradia, M., Vallance, J., Fontboté, L., Stein, H., Schaltegger, U., Coder, J., Richards, J. P., Villeneuve, M. & Gendall, I. (2009b). U–Pb, Re–Os, and $^{40}$Ar/$^{39}$Ar geochronology of the Nambija Au-skarn and Pangui porphyry Cu deposits, Ecuador: implications for the Jurassic metallogenic belt of the Northern Andes. *Mineralium Deposita* **44**, 371–387.

Chiaradia, M., Müntener, O. & Beate, B. (2011). Enriched basaltic andesites from mid-crustal fractional crystallization, re-charge, and assimilation (Pilavo volcano, western Cordillera of Ecuador). *Journal of Petrology* **52**, 1107–1141.

Chiaradia, M., Ulianov, A., Kouzmanov, K. & Beate, B. (2012). Why large porphyry Cu deposits like high Sr/Y magmas? *Scientific Reports* **2**, 685.

Chiaradia, M., Müntener, O. & Beate, B. (2014). Quaternary sanukitoid-like andesites generated by intracrustal processes (Chacana caldera complex, Ecuador): implications for Archean sanukitoids. *Journal of Petrology* **55**, 769–802.

Cloos, M. (2001). Bubbling magma chambers, cupolas, and porphyry copper deposits. *International Geology Review* **43**, 285–311.

Cooke, D. R., Hollings, P. & Walshe, J. L. (2005). Giant porphyry deposits: characteristics, distribution, and tectonic controls. *Economic Geology* **100**, 801–818.

Costa, F., Scaillet, B. & Pichavant, M. (2004). Petrological and experimental constraints on the pre-eruption conditions of Holocene dacite from Volcan San Pedro (36°S, Chilean Andes) and the importance of sulphur in silicic subduction-related magmas. *Journal of Petrology* **45**, 855–881.

Costa, F., Andreastuti, S., Bouvet de Maisonneuve, C. & Pallister, J. S. (2013). Petrological insights into the storage conditions, and magmatic processes that yielded the centennial 2010 Merapi explosive eruption. *Journal of Volcanology and Geothermal Research* **261**, 209–235.

de Hoog, J. C. M., Hattori, K. H. & Hoblitt, R. P. (2004). Oxidized sulfur-rich mafic magma at Mount Pinatubo, Philippines. *Contributions to Mineralogy and Petrology* **146**, 750–761.

DePaolo, D. J. (1981). Trace element and isotopic effects of combined wallrock assimilation and fractional crystallization. *Earth and Planetary Science Letters* **53**, 189–202.

Dilles, J. H. (1987). Petrology of the Yerington Batholith, Nevada; evidence for evolution of porphyry copper ore fluids. *Economic Geology* **82**, 1750–1789.

Dilles, J. H. & Proffett, J. M. (1995). Metallogenesis of the Yerington batholith, Nevada. In: Pierse, F. W. & Bolm, J. G. (eds) *Porphyry copper deposits of the American Cordillera. Arizona Geological Society Digest* **20**, 306–315.

Dreher, S. T., Macpherson, C. G., Pearson, D. G. & Davidson, J. P. (2005). Re–Os isotope studies of Mindanao adakites: Implications for sources of metals and melts. *Geology* **33**, 957–960.

Eichelberger, N., McQuarrie, N., Ryan, J., Karimi, B., Beck, S. & Zandt, G. (2015). Evolution of crustal thickening in the central Andes, Bolivia. *Earth and Planetary Science Letters* **426**, 191–203.

Engvik, A. K., Putnis, A., Fitz Gerald, J. D. & Austrheim, H. (2008). Albitization of granitic rocks: the mechanism of replacement of oligoclase by albite. *Canadian Mineralogist* **46**, 1401–1415.

Erdmann, S., Scaillet, B. & Kellett, D. A. (2010). Xenocryst assimilation and formation of peritectic crystals during magma contamination: An experimental study. *Journal of Volcanology and Geothermal Research* **198**, 355–367.

Erdmann, S., Martel, C., Pichavant, M. & Kushnir, A. (2014). Amphibole as an archivist of magmatic crystallization conditions: problems, potential, and implications for inferring magma storage prior to the paroxysmal 2010 eruption of Mount Merapi, Indonesia. *Contributions to Mineralogy and Petrology* **167**, 1016.

Evans, K. A. & Tomkins, A. G. (2011). The relationship between subduction zone redox budget and arc magma fertility. *Earth and Planetary Science Letters* **308**, 401–409.

Evans, K. A., Elburg, M. A. & Kamenetsky, V. S. (2012). Oxidation state of subarc mantle. *Geology* **40**, 783–786.

Frost, B. R., Chamberlain, K. R. & Schumacher, J. C. (2001). Sphene (titanite): phase relations and role as a geochronometer. *Chemical Geology* **172**, 131–148.

Glazner, A. F. (2007). Thermal limitations on incorporation of wall rock into magma. *Geology* **35**, 319–322.

Gotberg, N., McQuarrie, N. & Carlotto Caillaux, V. (2010). Comparison of crustal thickening budget and shortening estimates in southern Peru (12–14°S): Implications for mass balance and rotations in the 'Bolivian orocline.'. *Geological Society of America Bulletin* **122**, 727–742.

Gregory-Wodzicki, K. M. (2000). Uplift history of the Central and Northern Andes: A review. *Geological Society of America Bulletin* **112**, 1091–1105.

Halter, W. E., Pettke, T. & Heinrich, C. A. (2002). The origin of Cu/Au ratios in porphyry-type ore deposits. *Science* **296**, 1844–1846.

Halter, W. E., Heinrich, C. A. & Pettke, T. (2005). Magma evolution and the formation of porphyry Cu–Au ore fluids: evidence from silicate and sulfide melt inclusions. *Mineralium Deposita* **39**, 845–863.

Hattori, K. H. & Keith, J. (2001). Contribution of mafic melt to porphyry copper mineralization: evidence from Mount Pinatubo, Philippines, and Bingham Canyon, Utah, USA. *Mineralium Deposita* **36**, 799–806.

Hedenquist, J. W. & Lowenstern, J. B. (1994). The role of magmas in the formation of hydrothermal ore deposits. *Nature* **370**, 519–527.

Hindle, D., Kley, J., Oncken, O. & Sobolev, S. (2005). Crustal balance and crustal flux from shortening estimates in the Central Andes. *Earth and Planetary Science Letters* **230**, 113–124.

Holland, T. & Blundy, J. D. (1994). Non-ideal interactions in calcic amphiboles and their bearing on amphibole–plagioclase thermometry. *Contributions to Mineralogy and Petrology* **116**, 433–447.

Horton, B. K., Perez, N. D., Fitch, J. D. & Saylor, J. E. (2015). Punctuated shortening and subsidence in the Altiplano Plateau of southern Peru: Implications for early Andean mountain building. *Lithosphere* **7**, 117–137.

Hou, Z., Yang, Z., Qu, X., Meng, X., Li, Z., Beaudoin, G., Rui, Z., Gao, Y. & Zaw, K. (2009). The Miocene Gangdese porphyry copper belt generated during post-collisional extension in the Tibetan Orogen. *Ore Geology Reviews* **36**, 25–51.

Houston, R. A. & Dilles, J. H. (2013). Structural geologic evolution of the Butte district, Montana. *Economic Geology* **108**, 1397–1424.

Hövelmann, J., Putnis, A., Geisler, T., Schmidt, B. C. & Golla-Schindler, U. (2010). The replacement of plagioclase feldspars by albite: observations from hydrothermal experiments. *Contributions to Mineralogy and Petrology* **159**, 43–59.

Ishihara, S. (1981). The granitoid series and mineralization. *Economic Geology, 75th Anniversary Volume*, 458–484.

Jackson, S. (2008). LAMTRACE data reduction software for LA-ICP-MS. In: Sylvester, P. (ed.) *Laser Ablation ICP-MS in the Earth Sciences: Current Practices and Outstanding Issues.*

*Mineralogical Association of Canada, Short Course Series* **40**, 305–307.

Jugo, P. J. (2009). Sulfur content at sulfide saturation in oxidized magmas. *Geology* **37**, 415–418.

Jugo, P. J., Wilke, M. & Botcharnikov, R. E. (2010). Sulfur K-edge XANES analysis of natural and synthetic basaltic glasses: Implications for S speciation and S content as function of oxygen fugacity. *Geochimica et Cosmochimica Acta* **74**, 5926–5938.

Keith, J. D., Whitney, J. A., Hattori, K., Ballantyne, G. H., Christiansen, E. H., Barr, D. L., Cannan, T. M. & Hook, C. J. (1997). The role of magmatic sulfides and mafic alkaline magmas in the Bingham and Tintic mining districts, Utah. *Journal of Petrology* **38**, 1679–1690.

Kelley, K. A. & Cottrell, E. (2009). Water and the oxidation state of subduction zone magmas. *Science* **325**, 605–607.

Kennedy, B., Wilcock, J. & Stix, J. (2012). Caldera resurgence during magma replenishment and rejuvenation at Valles and Lake City calderas. *Bulletin of Volcanology* **74**, 1833–1847.

Lange, R. A., Frey, H. M. & Hector, J. (2009). A thermodynamic model for the plagioclase–liquid hygrometer/thermometer. *American Mineralogist* **94**, 494–506.

Leake, B. E., Woolley, A. R., Arps, C. E. S., et al. (1997). Nomenclature of amphiboles; report of the subcommittee on amphiboles of the International Mineralogical Association, Commission on New Minerals and Mineral Names. *Canadian Mineralogist* **35**, 219–246.

Lee, C.-T. A., Leeman, W. P., Canil, D. & A Li Z.-X., (2005). Similar V/Sc systematics in MORB and arc basalts: Implications for the oxygen fugacities of their mantle source regions. *Journal of Petrology* **46**, 2313–2336.

Lee, C.-T. A., Luffi, P., Le Roux, V., Dasgupta, R., Albarède, F. & Leeman, W. P. (2010). The redox state of arc mantle using Zn/Fe systematics. *Nature* **468**, 681–685.

Lee, C.-T. A., Luffi, P., Chin, E. J., Bouchet, R., Dasgupta, R., Morton, D. M., Le Roux, V., Yin, Q. Z. & Jin, D. (2012). Copper systematics in arc magmas and implications for crust–mantle differentiation. *Science* **336**, 64–68.

Loucks, R. R. (2014). Distinctive composition of copper-ore-forming arc magmas. *Australian Journal of Earth Sciences* **61**, 5–16.

Lynton, S. J., Candela, P. A. & Piccoli, P. M. (1993). An experimental study of the partitioning of copper between pyrrhotite and a high silica rhyolitic melt. *Economic Geology* **88**, 901–915.

Maher, K. C. (2010). Skarn alteration and mineralization at Coroccohuayco, Tintaya district, Peru. *Economic Geology* **105**, 263–283.

Mallmann, G. & O'Neill, H. St. C. (2009). The crystal/melt partitioning of V during mantle melting as a function of oxygen fugacity compared with some other elements (Al, P, Ca, Sc, Ti, Cr, Fe, Ga, Y, Zr and Nb). *Journal of Petrology* **50**, 1765–1794.

Mamani, M., Wörner, G. & Sempere, T. (2010). Geochemical variations in igneous rocks of the Central Andean orocline (13°S to 18°S): Tracing crustal thickening and magma generation through time and space. *Geological Society of America Bulletin* **122**, 162–182.

Marschall, H. R. & Schumacher, J. C. (2012). Arc magmas sourced from mélange diapirs in subduction zones. *Nature Geoscience* **5**, 862–867.

McCanta, M. C., Rutherford, M. J. & Hammer, J. E. (2007). Pre-eruptive and syn-eruptive conditions in the Black Butte, California dacite: Insight into crystallization kinetics in a silicic magma system. *Journal of Volcanology and Geothermal Research* **160**, 263–284.

McDonough, W. F. & Sun, S. S. (1995). The composition of the Earth. *Chemical Geology* **120**, 223–253.

McLeod, G. W., Dempster, T. J. & Faithfull, J. W. (2011). Deciphering magma-mixing processes using zoned titanite from the Ross of Mull Granite, Scotland. *Journal of Petrology* **52**, 55–82.

McQuarrie, N., Horton, B. K., Zandt, G., Beck, S. & DeCelles, P. G. (2005). Lithospheric evolution of the Andean fold–thrust belt, Bolivia, and the origin of the central Andean plateau. *Tectonophysics* **399**, 15–37.

Melekhova, E., Annen, C. & Blundy, J. D. (2013). Compositional gaps in igneous rock suites controlled by magma system heat and water content. *Nature Geoscience* **6**, 385–390.

Müntener, O. & Ulmer, P. (2006). Experimentally derived high-pressure cumulates from hydrous arc magmas and consequences for the seismic velocity structure of lower arc crust. *Geophysical Research Letters* **33**, L21308.

Müntener, O., Kelemen, P. B. & Grove, T. L. (2001). The role of $H_2O$ during crystallization of primitive arc magmas under uppermost mantle conditions and genesis of igneous pyroxenites: An experimental study. *Contributions to Mineralogy and Petrology* **141**, 643–658.

Nadeau, O., Williams-Jones, A. E. & Stix, J. (2010). Sulphide magma as a source of metals in arc-related magmatic hydrothermal ore fluids. *Nature Geoscience* **3**, 501–505.

Nakada, S. (1991). Magmatic processes in titanite-bearing dacites, central Andes of Chile and Bolivia. *American Mineralogist* **76**, 548–560.

Nandedkar, R. H., Ulmer, P. & Muentener, O. (2014). Fractional crystallization of primitive, hydrous arc magmas: an experimental study at 0·7 GPa. *Contributions to Mineralogy and Petrology* **167**, 1015.

Newman, S. & Lowenstern, J. B. (2002). VolatileCalc: a silicate melt–$H_2O$–$CO_2$ solution model written in Visual Basic for Excel. *Computers and Geosciences* **28**, 597–604.

Norberg, N., Neusser, G., Wirth, R. & Harlov, D. (2011). Microstructural evolution during experimental albitization of K-rich alkali feldspar. *Contributions to Mineralogy and Petrology* **162**, 531–546.

Oyarzun, R., Márquez, A., Lillo, J., López, I. & Rivera, S. (2001). Giant versus small porphyry copper deposits of Cenozoic age in northern Chile: adakitic versus normal calc-alkaline magmatism. *Mineralium Deposita* **36**, 794–798.

Panjasawatwong, Y., Danyushevsky, L. V., Crawford, A. J. & Harris, K. L. (1995). An experimental study of the effects of melt composition on plagioclase–melt equilibria at 5 and 10 kbar: implications for the origin of magmatic high-An plagioclase. *Contributions to Mineralogy and Petrology* **118**, 420–432.

Papale, P., Moretti, R. & Barbato, D. (2006). The compositional dependence of the saturation surface of $H_2O + CO_2$ fluids in silicate melts. *Chemical Geology* **229**, 78–95.

Perelló, J., Carlotto, V., Zarate, A., Ramos, P., Posso, H., Neyra, C., Caballero, A., Fuster, N. & Muhr, R. (2003). Porphyry-style alteration and mineralization of the Middle Eocene to Early Oligocene Andahuaylas–Yauri belt, Cuzco region, Peru. *Economic Geology* **98**, 1575–1605.

Pettke, T., Oberli, F. & Heinrich, C. A. (2010). The magma and metal source of giant porphyry-type ore deposits, based on lead isotope microanalysis of individual fluid inclusions. *Earth and Planetary Science Letters* **296**, 267–277.

Pichavant, M. & Macdonald, R. (2007). Crystallization of primitive basaltic magmas at crustal pressures and genesis of the calc-alkaline igneous suite: experimental evidence from St Vincent, Lesser Antilles arc. *Contributions to Mineralogy and Petrology* **154**, 535–558.

Pin, C., Briot, D., Bassin, C. & Poitrasson, F. (1994). Concomitant separation of strontium and samarium–neodymium for isotopic analysis in silicate samples, based on specific extraction chromatography. *Analytica Chimica Acta* **298**, 209–217.

Plank, T. (2005). Constraints from thorium/lanthanum on sediment recycling at subduction zones and the evolution of the continents. *Journal of Petrology* **46**, 921–944.

Plümper, O. & Putnis, A. (2009). The complex hydrothermal history of granitic rocks: multiple feldspar replacement reactions under subsolidus conditions. *Journal of Petrology* **50**, 967–987.

Powell, R. (1984). Inversion of the assimilation and fractional crystallization (AFC) equations; characterization of contaminants from isotope and trace element relationships in volcanic suites. *Journal of the Geological Society, London* **141**, 447–452.

Reitsma, M. J. (2012). Reconstructing the Late Paleozoic-Early Mesozoic plutonic and sedimentary record of south-east Peru: Orphaned back-arcs along the western margin of Gondwana. PhD thesis, Université de Genève, 246 pp.

Reubi, O. & Blundy, J. (2008). Assimilation of plutonic roots, formation of high-K 'exotic' melt inclusions and genesis of andesitic magmas at Volcán de Colima, Mexico. *Journal of Petrology* **49**, 2221–2243.

Reubi, O., Bourdon, B., Dungan, M. A., Koornneef, J. M., Sellés, D., Langmuir, C. H. & Aciego, S. (2011). Assimilation of the plutonic roots of the Andean arc controls variations in U-series disequilibria at Volcan Llaima, Chile. *Earth and Planetary Science Letters* **303**, 37–47.

Richards, J. P. (2003). Tectono-magmatic precursors for porphyry Cu–(Mo–Au) deposit formation. *Economic Geology* **98**, 1515–1533.

Richards, J. P. (2011a). High Sr/Y arc magmas and porphyry Cu ± Mo ± Au deposits: just add water. *Economic Geology* **106**, 1075–1081.

Richards, J. P. (2011b). Magmatic to hydrothermal metal fluxes in convergent and collided margins. *Ore Geology Reviews* **40**, 1–26.

Richards, J. P. (2013). Giant ore deposits formed by optimal alignments and combinations of geological processes. *Nature Geoscience* **6**, 911–916.

Richards, J. P. (2015). The oxidation state, and sulfur and Cu contents of arc magmas: implications for metallogeny. *Lithos* **233**, 27–45.

Richards, J. P. & Kerrich, R. (2007). Special Paper: Adakite-like rocks: their diverse origins and questionable role in metallogenesis. *Economic Geology* **102**, 537–576.

Richards, J. P., Spell, T., Rameh, E., Razique, A. & Fletcher, T. (2012). High Sr/Y magmas reflect arc maturity, high magmatic water content, and porphyry Cu ± Mo ± Au potential: examples from the Tethyan arcs of central and eastern Iran and western Pakistan. *Economic Geology* **107**, 295–332.

Ridolfi, F. & Renzulli, A. (2012). Calcic amphiboles in calc-alkaline and alkaline magmas: thermobarometric and chemometric empirical equations valid up to 1,130°C and 2·2 GPa. *Contributions to Mineralogy and Petrology* **163**, 877–895.

Rohrlach, B. D. & Loucks, R. R. (2005). Multi-million-year cyclic ramp-up of volatiles in a lower crustal magma reservoir trapped below the Tampakan copper–gold deposit by Mio-Pliocene crustal compression in the southern Philippines. In: Porter, T. M. (ed.) *Super Porphyry Copper and Gold Deposits: a Global Perspective*. PGC Publishing, pp. 369–407.

Roperch, P., Sempere, T., Macedo, O., Arriagada, C., Fornari, M., Tapia, C., García, M. & Laj, C. (2006). Counterclockwise

rotation of late Eocene–Oligocene fore-arc deposits in southern Peru and its significance for oroclinal bending in the central Andes. *Tectonics* **25**, TC3010.

Roperch, P., Carlotto, V., Ruffet, G. & Fornari, M. (2011). Tectonic rotations and transcurrent deformation south of the Abancay deflection in the Andes of southern Peru. *Tectonics* **30**, TC2010.

Rowe, M. C., Kent, A. J. R. & Nielsen, R. L. (2009). Subduction influence on oxygen fugacity and trace and volatile elements in basalts across the Cascade volcanic arc. *Journal of Petrology* **50**, 61–91.

Safran, E. B., Bierman, P. R., Aalto, R., Dunne, T., Whipple, K. X. & Caffee, M. (2005). Erosion rates driven by channel network incision in the Bolivian Andes. *Earth Surface Processes and Landforms* **30**, 1007–1024.

Sajona, F. G. & Maury, R. C. (1998). Association of adakites with gold and copper mineralization in the Philippines. *Comptes Rendus de l'Académie des Sciences, Série IIA* **326**, 27–34.

Sandeman, H. A., Clark, A. H. & Farrar, E. (1995). An integrated tectono-magmatic model for the evolution of the southern Peruvian Andes (13–20°S) since 55 Ma. *International Geology Review* **37**, 1039–1073.

Scaillet, B. & Evans, B. W. (1999). The 15 June 1991 eruption of Mount Pinatubo. I. Phase equilibria and pre-eruption $P$–$T$–$fO_2$–$fH_2O$ conditions of the dacite magma. *Journal of Petrology* **40**, 381–411.

Schmitt, A. K., Stockli, D. F., Lindsay, J. M., Robertson, R., Lovera, O. M. & Kislitsyn, R. (2010). Episodic growth and homogenization of plutonic roots in arc volcanoes from combined U–Th and (U–Th)/He zircon dating. *Earth and Planetary Science Letters* **295**, 91–103.

Schütte, P., Chiaradia, M., Barra, F., Villagómez, D. & Beate, B. (2011). Metallogenic features of Miocene porphyry Cu and porphyry-related mineral deposits in Ecuador revealed by Re–Os, [40]Ar/[39]Ar, and U–Pb geochronology. *Mineralium Deposita* **47**, 383–410.

Schütte, P., Chiaradia, M. & Beate, B. (2010). Petrogenetic evolution of arc magmatism associated with late Oligocene to late Miocene porphyry-related ore deposits in Ecuador. *Economic Geology* **105**, 1243–1270.

Seedorff, E., Dilles, J. H., Proffett, J. M., Einaudi, M. T., Zurcher, L., Stavast, W. J. A., Johnson, D. A. & Barton, M. D. (2005). Porphyry deposits: characteristics and origin of hypogene features. *Economic Geology, 100th Anniversary Volume*, 251–298.

Seedorff, E., Barton, M. D., Stavast, W. J. A. & Maher, D. J. (2008). Root zones of porphyry systems: extending the porphyry model to depth. *Economic Geology* **103**, 939–956.

Shafiei, B., Haschke, M. & Shahabpour, J. (2008). Recycling of orogenic arc crust triggers porphyry Cu mineralization in Kerman Cenozoic arc rocks, southeastern Iran. *Mineralium Deposita* **44**, 265–283.

Shen, P., Shen, Y., Liu, T., Meng, L., Dai, H. & Yang, Y. (2009). Geochemical signature of porphyries in the Baogutu porphyry copper belt, western Junggar, NW China. *Gondwana Research* **16**, 227–242.

Shinohara, H. & Hedenquist, J. W. (1997). Constraints on magma degassing beneath the Far Southeast porphyry Cu–Au deposit, Philippines. *Journal of Petrology* **38**, 1741–1752.

Sillitoe, R. H. (2010). Porphyry copper systems. *Economic Geology* **105**, 3–41.

Simakin, A. G. & Bindeman, I. N. (2012). Remelting in caldera and rift environments and the genesis of hot, 'recycled' rhyolites. *Earth and Planetary Science Letters* **337–338**, 224–235.

Simon, A. C. & Ripley, E. M. (2011). The role of magmatic sulfur in the formation of ore deposits. In: Behrens, H. & Webster, J. D. (eds) *Sulfur in Magmas and Melts: its Importance for Natural and Technical Processes. Mineralogical Society of America and Geochemical Society, Reviews in Mineralogy and Geochemistry* **73**, 513–578.

Sisson, T. W. & Grove, T. L. (1993a). Temperatures and $H_2O$ contents of low-MgO high-alumina basalts. *Contributions to Mineralogy and Petrology* **113**, 167–184.

Sisson, T. W. & Grove, T. L. (1993b). Experimental investigations of the role of $H_2O$ in calc-alkaline differentiation and subduction zone magmatism. *Contributions to Mineralogy and Petrology* **113**, 143–166.

Sisson, T. W., Ratajeski, K., Hankins, W. B. & Glazner, A. F. (2005). Voluminous granitic magmas from common basaltic sources. *Contributions to Mineralogy and Petrology* **148**, 635–661.

Skewes, M. A. & Stern, C. R. (1994). Tectonic trigger for the formation of late Miocene Cu-rich breccias in the Andes of central Chile. *Geology* **22**, 551–554.

Solano, J. M. S., Jackson, M. D., Sparks, R. S. J., Blundy, J. D. & Annen, C. (2012). Melt segregation in deep crustal hot zones: A mechanism for chemical differentiation, crustal assimilation and the formation of evolved magmas. *Journal of Petrology* **53**, 1999–2026.

Somoza, R. & Ghidella, M. E. (2012). Late Cretaceous to recent plate motions in western South America revisited. *Earth and Planetary Science Letters* **331–332**, 152–163.

Spera, F. J. & Bohrson, W. A. (2004). Open-system magma chamber evolution: an energy-constrained geochemical model incorporating the effects of concurrent eruption, recharge, variable assimilation and fractional crystallization (EC-E'RA$\chi$FC). *Journal of Petrology* **45**, 2459–2480.

Stavast, W. J. A. (2006). The fate of magmatic sulfides during intrusion or eruption, Bingham and Tintic districts, Utah. *Economic Geology* **101**, 329–345.

Stavast, W. J. A., Butler, R. F., Seedorff, E., Barton, M. D. & Ferguson, C. A. (2008). Tertiary tilting and dismemberment of the Laramide arc and related hydrothermal systems, Sierrita Mountains, Arizona. *Economic Geology* **103**, 629–636.

Steinberger, I., Hinks, D., Driesner, T. & Heinrich, C. A. (2013). Source plutons driving porphyry copper ore formation: combining geomagnetic data, thermal constraints, and chemical mass balance to quantify the magma chamber beneath the Bingham Canyon deposit. *Economic Geology* **108**, 605–624.

Stern, C. R., Skewes, M. A. & Arevalo, A. (2011). Magmatic evolution of the giant El Teniente Cu–Mo deposit, central Chile. *Journal of Petrology* **52**, 1591–1617.

Takagi, D., Sato, H. & Nakagawa, M. (2005). Experimental study of a low-alkali tholeiite at 1–5 kbar: optimal condition for the crystallization of high-An plagioclase in hydrous arc tholeiite. *Contributions to Mineralogy and Petrology* **149**, 527–540.

Tatsumi, Y. (1989). Migration of fluid phases and genesis of basalt magmas in subduction zones. *Journal of Geophysical Research* **94**, 4697–4707.

Tatsumi, Y., Hamilton, D. L. & Nesbitt, R. W. (1986). Chemical characteristics of fluid phase released from a subducted lithosphere and origin of arc magmas: Evidence from high-pressure experiments and natural rocks. *Journal of Volcanology and Geothermal Research* **29**, 293–309.

Thiéblemont, D., Stein, G. & Lescuyer, J.-L. (1997). Gisements épithermaux et porphyriques: la connexion adakite. *Comptes Rendus de l'Académie des Sciences, Série IIA* **325**, 103–109.

Thompson, A. B., Matile, L. & Ulmer, P. (2002). Some thermal constraints on crustal assimilation during fractionation of hydrous, mantle-derived magmas with examples from central Alpine batholiths. *Journal of Petrology* **43**, 403–422.

Tosdal, R. M. & Richards, J. P. (2001). Magmatic and structural controls on the development of porphyry Cu ± Mo ± Au deposits. In: Richards, J. P. & Tosdal, R. M. (eds) *Structural Controls on Ore Genesis. Reviews in Economic Geology*, 157–181.

Ulianov, A., Müntener, O., Schaltegger, U. & Bussy, F. (2012). The data treatment dependent variability of U–Pb zircon ages obtained using mono-collector, sector field, laser ablation ICPMS. *Journal of Analytical Atomic Spectrometry* **27**, 663–676.

Vigneresse, J.-L. (2007). The role of discontinuous magma inputs in felsic magma and ore generation. *Ore Geology Reviews* **30**, 181–216.

Walker, B. A., Klemetti, E. W., Grunder, A. L., Dilles, J. H., Tepley, F. J. & Giles, D. (2013). Crystal reaming during the assembly, maturation, and waning of an eleven-million-year crustal magma cycle: thermobarometry of the Aucanquilcha Volcanic Cluster. *Contributions to Mineralogy and Petrology* **165**, 663–682.

Wilkinson, J. J. (2013). Triggers for the formation of porphyry ore deposits in magmatic arcs. *Nature Geoscience* **6**, 917–925.

Wones, D. R. (1989). Significance of the assemblage titanite + magnetite + quartz in granitic rocks. *American Mineralogist* **74**, 744–749.

Workman, R. K. & Hart, S. R. (2005). Major and trace element composition of the depleted MORB mantle (DMM). *Earth and Planetary Science Letters* **231**, 53–72.

Xirouchakis, D. & Lindsley, D. H. (1998). Equilibria among titanite, hedenbergite, fayalite, quartz, ilmenite, and magnetite: Experiments and internally consistent thermodynamic data for titanite. *American Mineralogist* **83**, 712–725.

Zellmer, G. F., Iizuka, Y., Miyoshi, M., Tamura, Y. & Tatsumi, Y. (2012). Lower crustal $H_2O$ controls on the formation of adakitic melts. *Geology* **40**, 487–490.